

# Navigation from Low Earth Orbit – Part 2: Models, Implementation, and Performance

Zaher M. Kassas

# Table of Contents

<b>1</b>	<b>Introduction</b>	<b>1</b>
<b>2</b>	<b>LEO Satellite Pseudorange, Carrier Phase, and Doppler Measurement Model</b>	<b>3</b>
2.1	Pseudorange Measurement Model . . . . .	4
2.2	Doppler Measurement Model . . . . .	4
2.3	Carrier Phase Measurement Model . . . . .	4
<b>3</b>	<b>LEO Satellite Orbital Dynamics Model</b>	<b>5</b>
<b>4</b>	<b>Navigation Error Sources</b>	<b>7</b>
4.1	LEO Satellite Position and Velocity Error . . . . .	7
4.2	LEO Satellite Clock Errors . . . . .	8
4.3	Ionospheric and Tropospheric Errors . . . . .	9
<b>5</b>	<b>Overview of Orbcomm LEO Satellite Constellation</b>	<b>11</b>
5.1	Orbcomm System Overview . . . . .	11
5.2	Orbcomm Space Segment . . . . .	12
5.3	Orbcomm Downlink Signals . . . . .	13
5.4	Orbcomm Receiver Design . . . . .	13
<b>6</b>	<b>Overview of Starlink LEO Satellite Constellation</b>	<b>17</b>
6.1	Proposed Starlink Constellation . . . . .	17
6.2	Signal Information . . . . .	18
<b>7</b>	<b>Carrier Phase Differential Navigation with LEO Satellites Signals</b>	<b>18</b>
7.1	Framework Formulation . . . . .	19
7.2	Batch Navigation Solution . . . . .	20
<b>8</b>	<b>STAN: Simultaneous Tracking and Navigation with LEO Satellite Signals</b>	<b>21</b>
8.1	EKF State Vector and Dynamics Model . . . . .	22
8.1.1	EKF State Vector . . . . .	22
8.1.2	Vehicle Kinematics Model . . . . .	23
8.1.3	LEO Satellite Dynamics Model . . . . .	23
8.2	IMU Measurement Model and EKF Prediction . . . . .	23
8.3	Receiver Measurement Model and EKF Update . . . . .	24
<b>9</b>	<b>Dilution of Precision Analysis</b>	<b>24</b>
<b>10</b>	<b>Simulation Results</b>	<b>27</b>
10.1	Standalone Navigation Solution with LEO Satellite Signals . . . . .	27
10.2	LEO-Aided INS STAN . . . . .	28
10.2.1	UAV Simulation with Globalstar, Orbcomm, and Iridium LEO Constellations . . . . .	28

10.2.2 UAV Simulation with the Starlink LEO Constellation with Periodically Transmitted LEO Satellite Positions . . . . .	31
<b>11 Experimental Results</b>	<b>33</b>
11.1 Standalone Navigation Solution with LEO Satellite Signals . . . . .	33
11.2 CD-LEO Navigation Results . . . . .	34
11.3 LEO-Aided INS STAN . . . . .	36
11.3.1 Ground Vehicle . . . . .	36
11.3.2 Aerial Vehicle . . . . .	38

# 1 Introduction

The promise of broadband low Earth orbit (LEO) satellite signals for positioning, navigation, and timing (PNT) has been demonstrated in the past decade [1–7]. While some LEO-based PNT approaches require tailoring the broadband protocol to support PNT capabilities [3, 5, 8], other approaches exploit LEO constellations for PNT in an opportunistic fashion [2, 4, 9–11]. The former approaches allow for simpler receiver architectures and navigation algorithms. However, they require significant changes to existing infrastructure, the cost of which private companies, which are planning to aggregately launch tens of thousands of broadband Internet satellites into LEO, may not be willing to pay. Moreover, if these companies agree to that additional cost, there will be no guarantees that they would not charge for “extra navigation services.” In this case, exploiting broadband LEO satellite signals opportunistically for navigation becomes the more attractive approach.

Opportunistic navigation, or navigation with signals of opportunity (SOPs), has been recently considered as a reliable alternative paradigm to GNSS navigation [12–15]. Besides broadband LEO satellite signals, other SOPs include AM/FM radio [16–19], Wi-Fi [20–23], digital television [24–26], and cellular [27–34], with the latter showing a standalone meter-level-accurate navigation solution on ground vehicles [33, 35–39] and a centimeter-level-accurate navigation solution on aerial vehicles [40–42]. Moreover, SOPs have been used as an aiding source for lidar [43, 44] and an inertial navigation system (INS) [45–53].

LEO satellites possess desirable attributes for PNT. First, LEO satellites are around twenty-times closer to Earth compared to GNSS satellites that reside in medium Earth orbit (MEO), making LEO satellites’ received signals significantly more powerful. Second, LEO satellites orbit the Earth at much faster rates compared to GNSS satellites, making LEO satellites’ Doppler measurements attractive to exploit. Third, announcements by OneWeb, SpaceX (Starlink), Boeing, Samsung, Kepler, Telesat, and LeoSat, among others, to provide broadband Internet to the world via satellites will collectively bring tens of thousands of new LEO satellites into operation over the next decade, making their signals abundant and diverse in frequency and direction [3, 54, 55]. Figure 1 depicts a subset of existing and future LEO satellite constellations.

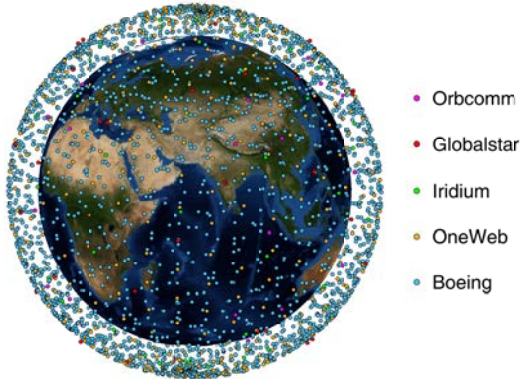


Figure 1: Existing and future LEO satellite constellations.

Table 1 summarizes the number of satellites and the transmission band of each constellation.

Table 1: Existing and future LEO constellations: number of satellite and transmission bands.

<b>System</b>	<b>Number of satellites</b>	<b>Frequency band</b>
Orbcomm	36	VHF
Globalstar	48	S and C
Iridium	66	L and Ka
OneWeb	882	Ku and Ka
Boeing	2956	V and C
SpaceX	11943	Ku, Ka, and V
Samsung	4600	V

To use LEO satellite signals for PNT, the satellites’ positions, velocities, and clock states must be determined. The position and velocity of any satellite may be parameterized by its Keplerian elements: eccentricity, semi-major axis, inclination, longitude of the ascending node, argument of periapsis, and true anomaly. With time, these orbital elements will drift from their nominal values due to several perturbing forces acting on the LEO satellite. In contrast to GNSS, where corrections to the orbital elements and clock errors are periodically transmitted to the receiver in the navigation message, such orbital element and clock corrections may not be available for LEO satellites; in which case they must be estimated. An orbit propagator and initialization scheme should be selected to carry out this estimation problem. Orbit propagators consist of equations of motion governed by force models, which fall into two main categories: analytical and numerical [56]. The difference between propagators in these two categories is apparent in their trade-off between accuracy and computational complexity. On one hand, analytical propagators reduce model fidelity, which in turn degrades the propagation accuracy, in order to achieve a computationally efficient analytical solution. On the other hand, numerical approaches achieve higher accuracy by performing costly numerical integrations of complicated force models. For instance, the LEO analytical propagator, known as the simplified general perturbations 4 (SGP4) model, uses two-line element (TLE) files that contain orbital elements and corrective terms to initialize and propagate the position and velocity of a satellite [57]. TLEs are produced daily by the North American Aerospace Defense Command (NORAD) to support the on-going usage of SGP4 as an orbit determination method. The information in TLE files can be used to initialize any simplified general perturbation (SGP) model to propagate a satellite in its orbit. However, the simplified models of perturbing forces, which include non-uniform Earth gravitational field, atmospheric drag, solar radiation pressure, third-body gravitational forces (e.g., gravity of the Moon and Sun), and general relativity, cause errors in a propagated satellite orbit around three to ten-kilometers, 24-hours after a TLE is produced [56]. In contrast, numerical propagators, also known as precise orbit determination (POD) methods, yield accurate ephemerides with errors on the order of tens-of-meters, in the radial, along-

track, and cross-track directions for a satellite, with more error occurring in the along-track direction [56, 58]. Unlike SGP propagators, POD propagators do not have a TLE-equivalent initialization file that is publicly available.

The exploitation of LEO satellites for PNT has been considered in other contexts. In [59], *simulated* LEO satellite Doppler measurements from *known* satellite positions were used to complement a cellular radio frequency pattern matching algorithm for localizing emergency 911 callers. In [60], *simulated* Doppler measurements from one LEO satellite with *known* position and velocity were used to localize a receiver. In [61], the position, velocity, and clock errors of a receiver were estimated using *simulated* LEO satellite time-difference of arrival (TDOA) and frequency-difference of arrival (FDOA) measurements using a reference receiver with a known position.

In contrast to the aforementioned approaches, which make the impractical assumption of perfectly knowing LEO satellite states; a practical, yet sophisticated approach is to estimate the poorly known LEO satellite states simultaneously with the navigating receiver's states. This approach, termed STAN: simultaneous tracking and navigation, was proposed in [4, 6, 7, 9, 11]. STAN is analogous to radio simultaneous localization and mapping (radio SLAM) [45, 53, 62–66], which consider *stationary* terrestrial signals of opportunity transmitters, with the added complexity of tracking the *mobile* LEO transmitters' states. Upon making pseudorange and Doppler LEO measurements, STAN can produce a navigation solution in (i) a standalone fashion [10, 67] or (ii) an integrated fashion, by aiding the INS [4, 6, 7, 9, 11].

This chapter is organized as follows. Section 2 describes the LEO satellite pseudorange, carrier phase, and Doppler frequency measurement models. Section 3 gives a brief overview of LEO satellite orbital dynamics models. Section 4 overviews sources of error for LEO satellite-based navigation. Section 5 overviews the existing Orbcomm LEO constellation and presents a receiver design for obtaining Doppler measurements from this constellation. Section 6 overviews the proposed Starlink LEO constellation. Section 7 presents a carrier phase differential framework for navigation with LEO satellites. Section 8 presents the STAN framework. Section 9 analyzes the dilution of precision with the existing Orbcomm and future Starlink LEO satellite constellations. Section 10 presents simulation results demonstrating the expected performance with existing and future LEO satellite constellations. Section 11 presents LEO-based experimental navigation results on a stationary receiver as well as ground and aerial vehicles.

## 2 LEO Satellite Pseudorange, Carrier Phase, and Doppler Measurement Model

This section describes the LEO satellite receiver pseudorange, carrier phase, and Doppler measurement model.

## 2.1 Pseudorange Measurement Model

A LEO receiver extracts pseudorange measurements  $\rho$  from LEO satellites by estimating the time-of-arrival. The pseudorange  $\rho_l$  from the  $l$ -th LEO satellite at time-step  $k$ , which represents discrete-time at  $t_k = kT + t_0$  for an initial time  $t_0$  and sampling time  $T$ , is modeled as

$$\rho_l(k) = \|\mathbf{r}_r(k) - \mathbf{r}_{\text{leo}_l}(k')\|_2 + c \cdot [\delta t_r(k) - \delta t_{\text{leo}_l}(k')] + c\delta t_{\text{iono}_l}(k) + c\delta t_{\text{tropo}_l}(k) + v_{\rho_l}(k), \quad (1)$$

$$l = 1, \dots, L, \quad k = 1, 2, \dots,$$

where  $k'$  represents discrete-time at  $t_k = kT + t_0 - \delta t_{\text{TOF}_l}$ , with  $\delta t_{\text{TOF}_l}$  being the true time-of-flight of the signal from the  $l$ -th LEO satellite;  $\mathbf{r}_r$  and  $\mathbf{r}_{\text{leo}_l}$  are the LEO receiver's and  $l$ -th LEO satellite's three-dimensional (3-D) position vectors, respectively;  $\delta t_r$  and  $\delta t_{\text{leo}_l}$  are the LEO receiver and the  $l$ -th LEO satellite transmitter clock biases, respectively;  $\delta t_{\text{iono}_l}$  and  $\delta t_{\text{tropo}_l}$  are the ionospheric and tropospheric delays, respectively, affecting the  $l$ -th LEO satellite's signal;  $L$  is the total number of visible LEO satellites; and  $v_{\rho_l}$  is the pseudorange measurement noise, which is modeled as a white Gaussian random sequence with variance  $\sigma_{v_{\rho,l}}^2$ .

## 2.2 Doppler Measurement Model

A LEO receiver extracts Doppler frequency measurements  $f_D$  from LEO satellites by differencing the nominal carrier frequency and the received signal frequency. A pseudorange rate measurement  $\dot{\rho}$  can be obtained from

$$\dot{\rho} = -\frac{c}{f_c} f_D,$$

where  $c$  is the speed of light and  $f_c$  is the carrier frequency.

A pseudorange rate measurement  $\dot{\rho}$  from the  $l$ -th LEO satellite is given by

$$\begin{aligned} \dot{\rho}_l(k) = & [\dot{\mathbf{r}}_r(k) - \dot{\mathbf{r}}_{\text{leo}_l}(k')] \frac{[\mathbf{r}_r(k) - \mathbf{r}_{\text{leo}_l}(k')]}{\|\mathbf{r}_r(k) - \mathbf{r}_{\text{leo}_l}(k')\|_2} + c \cdot [\dot{\delta t}_r(k) - \dot{\delta t}_{\text{leo}_l}(k')] \\ & + c\dot{\delta t}_{\text{iono}_l}(k) + c\dot{\delta t}_{\text{tropo}_l}(k) + v_{\dot{\rho}_l}(k), \quad l = 1, \dots, L, \quad k = 1, 2, \dots, \end{aligned} \quad (2)$$

where  $\dot{\mathbf{r}}_r$  and  $\dot{\mathbf{r}}_{\text{leo}_l}$  are the LEO receiver's and  $l$ -th LEO satellite's 3-D velocity vectors, respectively;  $\dot{\delta t}_r$  and  $\dot{\delta t}_{\text{leo}_l}$  are the LEO receiver and the  $l$ -th LEO satellite transmitter clock drifts, respectively;  $\dot{\delta t}_{\text{iono}_l}$  and  $\dot{\delta t}_{\text{tropo}_l}$  are the drifts of the ionospheric and tropospheric delays, respectively, affecting the  $l$ -th LEO satellite's signal; and  $v_{\dot{\rho}_l}$  is the pseudorange rate measurement noise, which is modeled as a white Gaussian random sequence with variance  $\sigma_{v_{\dot{\rho},l}}^2$ .

## 2.3 Carrier Phase Measurement Model

The continuous-time carrier phase observable can be obtained by integrating the Doppler measurement over time [68]. The carrier phase (expressed in cycles) made by the  $i$ -th receiver

on the  $l$ -th LEO satellite is given by

$$\varphi_l^{(i)}(t) = \varphi_l^{(i)}(t_0) + \int_{t_0}^t f_{D_l}^{(i)}(\tau) d\tau, \quad l = 1, \dots, L, \quad (3)$$

where  $f_{D_l}^{(i)}$  is the Doppler measurement made by the  $i$ -th receiver on the  $l$ -th LEO satellite and  $\varphi_l^{(i)}(t_0)$  is the initial carrier phase. To achieve a highly precise navigation solution, differential techniques from a base and a rover receiver can be employed. In (3),  $i$  denotes either the base B or the rover R. Assuming a constant Doppler during a subaccumulation period  $T$ , (3) can be discretized to yield

$$\varphi_l^{(i)}(k) = \varphi_l^{(i)}(0) + \sum_{n=0}^{k-1} f_{D_l}^{(i)}(n)T, \quad l = 1, \dots, L, \quad k = 1, 2, \dots \quad (4)$$

Note that the receiver will make noisy carrier phase measurements. Adding measurement noise and denoting  $\phi_l^{(i)}(k) \triangleq \lambda_l \varphi_l^{(i)}(k)$  to be the carrier phase observable in meters, where  $\lambda_l$  is the wavelength of the carrier signal transmitted by the  $l$ -th LEO satellite, yields the carrier phase measurement model (expressed in meters) given by

$$\phi_l^{(i)}(k) = \phi_l^{(i)}(0) + \lambda_l T \sum_{n=0}^{k-1} f_{D_l}^{(i)}(n) + v_l^{(i)}(k), \quad l = 1, \dots, L, \quad k = 1, 2, \dots, \quad (5)$$

where  $v_l^{(i)}(k)$  is the measurement noise, which is modeled as a zero-mean white Gaussian random sequence with variance  $\left[\sigma_l^{(i)}(k)\right]^2$ .

The carrier phase in (5) can be parameterized in terms of the receiver and LEO satellite states as

$$\begin{aligned} \phi_l^{(i)}(k) = & \|\mathbf{r}_{r_i}(k) - \mathbf{r}_{\text{leo}_l}(k'_l)\|_2 + c[\delta t_{r_i}(k) - \delta t_{\text{leo}_l}(k'_l)] + \lambda_l N_l^{(i)} \\ & + c\delta t_{\text{trop},l}^{(i)}(k) + c\delta t_{\text{iono},l}^{(i)}(k) + v_l^{(i)}(k), \quad l = 1, \dots, L, \quad k = 1, 2, \dots, \end{aligned} \quad (6)$$

where  $\mathbf{r}_{r_i}$  is the  $i$ -th receiver's position vector and  $N_l^{(i)}$  is the carrier phase ambiguity.

### 3 LEO Satellite Orbital Dynamics Model

This section gives a brief overview of LEO satellite orbital dynamics, which are used in the navigation filter to estimate the LEO satellites' states in the STAN framework. To this end, a simplified two-body model for the position and velocity dynamics of the LEO satellite will be used. The two-body motion equation of the  $l$ -th LEO satellite is given by

$$\ddot{\mathbf{r}}_{\text{leo}_l}(t) = -\frac{\mu}{\|\mathbf{r}_{\text{leo}_l}(t)\|_2^3} \mathbf{r}_{\text{leo}_l}(t) + \tilde{\mathbf{w}}_{\text{leo}_l}(t), \quad (7)$$

where  $\ddot{\mathbf{r}}_{\text{leo}_l}(t) = \frac{d}{dt} \dot{\mathbf{r}}_{\text{leo}_l}(t)$ , i.e., the acceleration of the  $l$ -th LEO satellite,  $\mu$  is the standard gravitational parameter, and  $\tilde{\mathbf{w}}_{\text{leo}_l}$  is process noise, which attempts to capture the overall

perturbation in acceleration, which includes non-uniform Earth gravitational field, atmospheric drag, solar radiation pressure, third-body gravitational forces (e.g., gravity of the Moon and Sun), and general relativity [56]. The process noise vector  $\tilde{\mathbf{w}}_{\text{leo}_l}$  is modeled as a white random vector with power spectral density (PSD)  $\mathbf{Q}_{\tilde{\mathbf{w}}_{\text{leo}_l}}$ . The two-body model (7) is convenient because it has a known analytical solution; however, the perturbing accelerations are not zero mean, which this model neglects. Omitting these perturbing accelerations can cause hundreds of meters in position error after just a few minutes of open-loop propagation due to the model mismatch [7].

While the two-body model has a known and simple analytical Jacobian for estimation error covariance propagation, the accumulation of position and velocity estimation error is large, especially for large intervals between measurement epochs. Furthermore, since the process noise vector  $\tilde{\mathbf{w}}_{\text{leo}_l}$  is modeled as a white process, which is attempting to capture unmodeled perturbations, the PSD  $\mathbf{Q}_{\tilde{\mathbf{w}}_{\text{leo}_l}}$  would have to be selected to over-bound these expected perturbations. This over bounding can cause a model mismatch, which can lead to incorrect propagation of the estimation error covariance, and subsequently cause inconsistent estimation or filter divergence altogether.

A more sophisticated LEO satellite orbital dynamics model can be used, which significantly reduces estimation errors by including the most significant non-zero mean perturbing acceleration components, while maintaining a simple analytical Jacobian for estimation error covariance propagation. The most significant perturbing accelerations for a LEO satellite is due to Earth's non-uniform gravity  $\mathbf{a}_{\text{grav}}$ . The two-body model with  $\mathbf{a}_{\text{grav}}$  can be written more generally as

$$\ddot{\mathbf{r}}_{\text{leo}_l}(t) = \mathbf{a}_{\text{grav}_l}(t), \quad \mathbf{a}_{\text{grav}_l}(t) = \frac{dU_l(t)}{d\mathbf{r}_{\text{leo}_l}(t)}, \quad (8)$$

where  $U_l$  is the non-uniform gravity potential of the Earth.

To model the non-uniform gravity potential of the Earth  $U_l$ , several models have been developed. For a satellite requiring accuracies of a few meters, the JGM-3 model developed by Goddard Space Flight Center is usually sufficient [69]. In this work, the tesseral and sectoral terms of the JGM-3 model are neglected, since they are several orders of magnitude smaller than the zonal terms (denoted  $\{J_n\}_{n=2}^{\infty}$ ). This gives the gravitational potential of the Earth at the  $l$ -th LEO satellite as [70]

$$U_l(t) = \frac{\mu}{\|\mathbf{r}_{\text{leo}_l}(t)\|} \left[ 1 - \sum_{n=2}^N J_n \frac{R_E^n}{\|\mathbf{r}_{\text{leo}_l}(t)\|^n} P_n[\sin(\theta)] \right], \quad (9)$$

where  $P_n$  is a Legendre polynomial with harmonic  $n$ ,  $J_n$  is the  $n^{\text{th}}$  zonal coefficient,  $R_E$  is the mean radius of the Earth,  $\sin(\theta) = z_{\text{leo}_l}/\|\mathbf{r}_{\text{leo}_l}\|$ ,  $\mathbf{r}_{\text{leo}_l} \triangleq [x_{\text{leo}_l}, y_{\text{leo}_l}, z_{\text{leo}_l}]^T$  is the position vector of the  $l$ -th LEO satellite in an Earth-centered inertial frame, and  $N = \infty$ . The terms of acceleration corresponding to coefficients  $> J_2$  are approximately three orders of magnitude smaller than the ones due to  $J_2$ . Therefore, the perturbation due to non-uniform gravity will be approximated by using only the term corresponding to  $J_2$ . Taking the partial

derivative of (9) with respect to the components of  $\mathbf{r}_{\text{leo}_l}$  with  $N \equiv 2$  gives the components of  $\mathbf{a}_{\text{grav}_l} = [\ddot{x}_{\text{grav}_l}, \ddot{y}_{\text{grav}_l}, \ddot{z}_{\text{grav}_l}]^T$  to be

$$\begin{aligned}\ddot{x}_{\text{grav}_l}(t) &= -\frac{\mu x_{\text{leo}_l}(t)}{\|\mathbf{r}_{\text{leo}_l}(t)\|^3} \left[ 1 + J_2 \frac{3}{2} \left( \frac{R_e}{\|\mathbf{r}_{\text{leo}_l}(t)\|} \right)^2 \left( 1 - 5 \frac{z_{\text{leo}_l}^2(t)}{\|\mathbf{r}_{\text{leo}_l}(t)\|^2} \right) \right], \\ \ddot{y}_{\text{grav}_l}(t) &= -\frac{\mu y_{\text{leo}_l}(t)}{\|\mathbf{r}_{\text{leo}_l}(t)\|^3} \left[ 1 + J_2 \frac{3}{2} \left( \frac{R_e}{\|\mathbf{r}_{\text{leo}_l}(t)\|} \right)^2 \left( 1 - 5 \frac{z_{\text{leo}_l}^2(t)}{\|\mathbf{r}_{\text{leo}_l}(t)\|^2} \right) \right], \\ \ddot{z}_{\text{grav}_l}(t) &= -\frac{\mu z_{\text{leo}_l}(t)}{\|\mathbf{r}_{\text{leo}_l}(t)\|^3} \left[ 1 + J_2 \frac{3}{2} \left( \frac{R_e}{\|\mathbf{r}_{\text{leo}_l}(t)\|} \right)^2 \left( 3 - 5 \frac{z_{\text{leo}_l}(t)^2}{\|\mathbf{r}_{\text{leo}_l}(t)\|^2} \right) \right].\end{aligned}\quad (10)$$

Further analysis comparing different LEO orbital dynamic models can be found in [7].

## 4 Navigation Error Sources

This section discusses error sources affecting the navigation performance of the STAN framework, namely: (i) imperfect knowledge of LEO satellite position and velocity states, (ii) unknown LEO satellites' clock error states, and (iii) ionospheric and tropospheric errors. In order to visualize the effect of (i) the satellite position and velocity errors, (ii) the clock drift error, and (iii) the ionospheric delay rates, the residual error between the measured pseudorange rate and the pseudorange rate estimated from the satellite position and velocity obtained from TLE files and SGP4 are plotted in Figure 2 for two Orbcomm satellites (FM 108 and FM 116). The following subsections discuss each of these error sources separately.

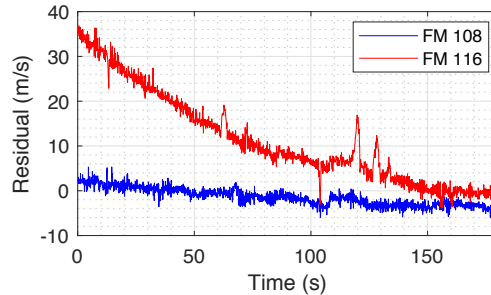


Figure 2: Residual errors showing the effect of (i) satellite position and velocity errors, (ii) clock errors, and (iii) ionospheric delay rates for 2 Orbcomm LEO satellites.

### 4.1 LEO Satellite Position and Velocity Error

One source of error that should be considered when navigating with LEO satellite signals arises due to imperfect knowledge of the LEO satellites' position and velocity. This is due to time-varying Keplerian elements caused by several perturbing accelerations acting on the satellite. Mean Keplerian elements and perturbing acceleration parameters are contained in publicly available TLE file sets which can be used to initialize SGP propagators designed to

propagate a LEO satellite’s orbit. SGP propagators (e.g., SGP4) are optimized for speed by replacing complicated perturbing acceleration models that require numerical integrations with analytical expressions to propagate a satellite position from an epoch time to a specified future time. The tradeoff is in satellite position accuracy: the SGP4 propagator has around 3 km in position error at epoch and the propagated orbit will continue to deviate from its true one until the TLE files are updated the following day. Figure 3 shows the accumulated position and velocity error for an Orbcomm LEO satellite (FM 112).

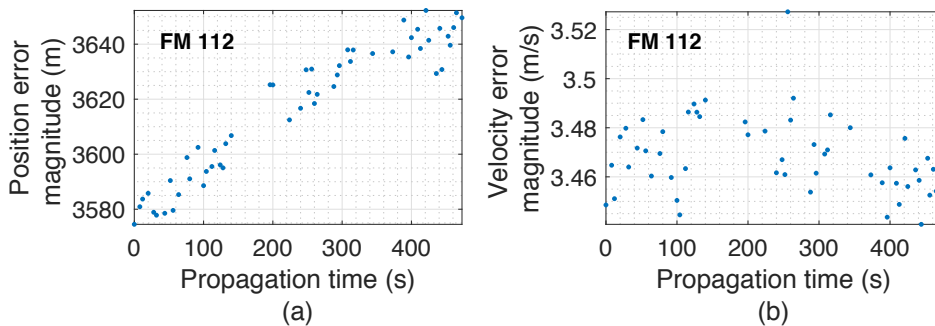


Figure 3: SGP4 (a) position and (b) velocity errors.

## 4.2 LEO Satellite Clock Errors

In contrast to GNSS, LEO satellite clocks are not tightly synchronized and the clock errors (bias and drift) are unknown to the receiver. Moreover, LEO satellites are not necessarily equipped with high-quality atomic clocks. From what is known about the existing LEO constellations, LEO satellites are equipped with oven-controlled crystal oscillators (OCXOs). Practically, the navigating receiver will be equipped with a lower quality oscillator, e.g., a temperature-compensated crystal oscillator (TCXO). To visualize the magnitude of the clock errors in the satellite and receiver clocks, Figure 3 depicts the time evolution of the  $1-\sigma$  bound of the clock bias and drift of a typical OCXO and a typical TCXO, obtained from the so-called two-state clock model [71]. It can be seen from Figure 3 that the satellite and receiver clock bias and drift may become very significant; therefore, they must be accounted for appropriately.

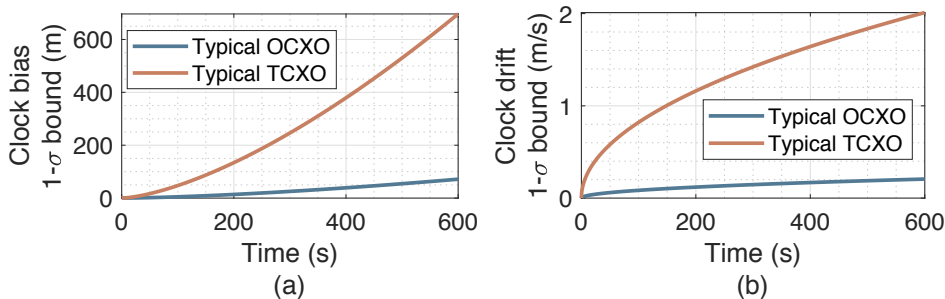


Figure 4: Time evolution of  $1-\sigma$  bounds of (a) clock bias and (b) clock drift for a typical OCXO and a typical TCXO over a 10-minute period.

### 4.3 Ionospheric and Tropospheric Errors

Most broadband LEO constellations reside above the ionosphere, which in turn will induce delays into their signals. Although LEO satellite signals propagate through the troposphere, its effect is less significant compared to ionospheric propagation. This subsection discusses the effect of propagating through the ionosphere and troposphere on pseudorange and pseudorange rate measurements, which are captured by the ionospheric and tropospheric delay and delay rates, respectively.

The magnitude of the ionospheric delay rate is (i) inversely proportional to the square of the carrier frequency and (ii) proportional to the rate of change of the obliquity factor, which is determined by the time evolution of the satellite's elevation angle. Note that the ionospheric delay rates also depend on the rate of change of the total electron content (TEC) at zenith, denoted by TECV. However, TECV varies much slower than the satellite's elevation angle; hence, its effect may be ignored. The effect of ionospheric propagation is significant on LEO satellite signals since (i) the high speed of LEO satellites translates into very fast changing elevation angles, as shown in Figure 5 and (ii) some of the existing LEO satellites transmit in the VHF band, where the signals experience very large delay rates.

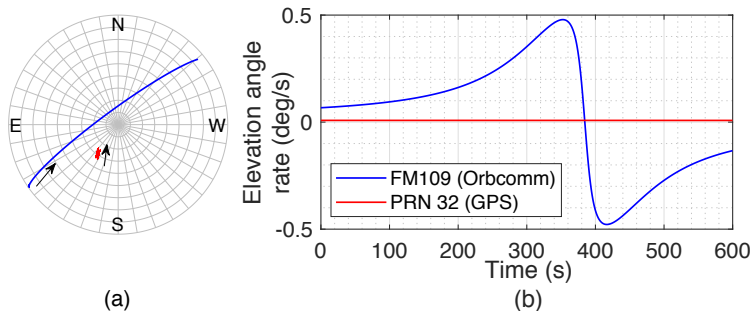


Figure 5: (a) Skyplot showing the trajectory of an Orbcomm LEO satellite (FM 109) and a GPS MEO satellite (PRN 32) over a 10-minute period. (b) The elevation angle rate of FM 109 and PRN 32 over the 10-minute trajectory. The elevation angle rate of the Orbcomm LEO satellite reaches as high as 60 times that of the GPS MEO satellite.

To study the ionospheric and tropospheric delay rates for LEO satellites, the ionospheric and tropospheric delays are first investigated and then their time derivative is taken to compute the rates. For radio frequency signals transmitted at a carrier exceeding 1 MHz, the excess phase delay due to propagation in the ionosphere can be approximated by

$$\delta t_{\text{iono},l}^{(i)}(k) = \frac{40.3 \times 10^{16} \times \alpha_{\text{iono}} \left( \theta_l^{(i)}(k) \right) \times \text{TECV}^{(i)}(k)}{c f_{c,l}^2}, \quad (11)$$

where  $\theta_l^{(i)}(k)$  is the elevation angle of the  $l$ -th LEO satellite with respect to the  $i$ -th receiver at time-step  $k$ ;  $f_{c,l}$  is the  $l$ -th LEO satellite's carrier frequency;  $\alpha_{\text{iono}}(\cdot)$  is the obliquity factor for a given elevation angle; and  $\text{TECV}^{(i)}(k)$  is the total electron count at the  $i$ -th receiver's zenith (i.e., when the elevation angle is  $\pi/2$ ) [68]. Note that  $\text{TECV}^{(i)}(k)$  in (11) is expressed

in TEC Units (TECU), which is defined as  $10^{16}$  electrons/m<sup>2</sup>, and is assumed to be constant during satellite visibility. Note that a map for TECV for the  $i$ -th receiver's location at different times can be accessed online [72]. The obliquity factor is given by

$$\alpha_{\text{iono}}(u) = \left[ 1 - \left( \frac{R_E \cos u}{R_E + h_I} \right)^2 \right]^{-\frac{1}{2}},$$

where  $R_E$  is the average radius of the Earth and  $h_I$  is the mean ionospheric height, which is taken to be 350 km.

Tropospheric delays can be modeled as the sum of two terms: dry gases in the atmosphere and the second due to water vapor in the atmosphere. The corresponding delays are called dry and wet delays, respectively, and the total tropospheric delay is modeled as

$$\delta t_{\text{trop},l}^{(i)}(k) = \delta t_{z,w}^{(i)} \alpha_{\text{trop},w} \left( \theta_l^{(i)}(k) \right) + \delta t_{z,d}^{(i)} \alpha_{\text{trop},d} \left( \theta_l^{(i)}(k) \right), \quad (12)$$

where  $\delta t_{z,w}^{(i)}$  and  $\delta t_{z,d}^{(i)}$  are the wet and dry delays at the  $i$ -th receiver's zenith, respectively, and  $\alpha_{\text{trop},w}(\cdot)$  and  $\alpha_{\text{trop},d}(\cdot)$  are the wet and dry tropospheric obliquity factors, respectively. The obliquity factors may be approximated by

$$\alpha_{\text{trop},w}(u) = \frac{1}{\sin u + \frac{0.00035}{\tan u + 0.017}},$$

$$\alpha_{\text{trop},d}(u) = \frac{1}{\sin u + \frac{0.00143}{\tan u + 0.0445}}.$$

Using the Hopfield model, the wet and dry delays may be approximated with

$$\delta t_{z,w}^{(i)} = 0.373 \frac{e_0^{(i)}}{c \left( T_0^{(i)} \right)^2} \frac{h_w}{5}, \quad \delta t_{z,d}^{(i)} = 77.6 \times 10^{-6} \frac{P_0^{(i)}}{c T_0^{(i)}} \frac{h_d}{5},$$

where  $T_0^{(i)}$  is the temperature (kelvin),  $P_0^{(i)}$  is the total pressure and  $e_0^{(i)}$  is the partial pressure due to water vapor (both in millibars),  $h_w = 12$  km, and  $h_d \approx 43$  km [68].

Fig. 6 shows the sum of simulated ionospheric and tropospheric delays for 5 Orbcomm LEO satellites transmitting in the very-high frequency (VHF) band and 5 GPS satellites at L1 frequency over a 4-hour period. It can be seen that the ionospheric delays for Orbcomm satellites are orders of magnitude higher than those of GPS satellites due to the difference in transmit frequency. The aforementioned factors result in large ionospheric delay rates, as shown in Figure 7 for 7 Orbcomm satellites over a 100-minute period.

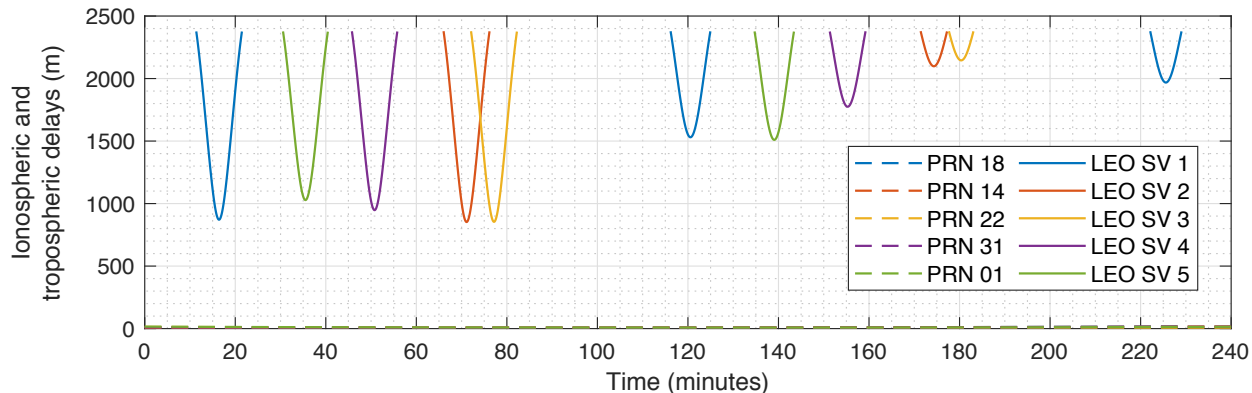


Figure 6: Simulated delays in meters due to ionosphere and troposphere propagation for 5 Orbcomm LEO satellites and 5 GPS satellites.

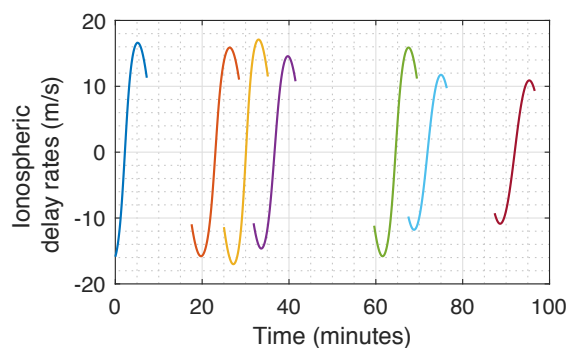


Figure 7: Ionospheric delay rates (expressed in m/s) for 7 Orbcomm satellites over a 100-minute period. Each color corresponds to a different Orbcomm LEO satellite.

## 5 Overview of Orbcomm LEO Satellite Constellation

This section overviews the existing Orbcomm LEO satellite constellation and describes how to estimate Doppler measurements these satellites.

### 5.1 Orbcomm System Overview

The Orbcomm system is a wide area two-way communication system that uses a constellation of LEO satellites to provide worldwide geographic coverage for sending and receiving alphanumeric packets [73]. The Orbcomm system consists of three main segments: (i) subscriber communicators (users), (ii) ground segment (gateways), and (iii) space segment (constellation of satellites). These segments are briefly discussed next.

- i. **Subscriber Communicators (SCs):** There are several types of SCs. Orbcomm’s SC for fixed data applications uses low-cost VHF electronics. The SC for mobile two-way messaging is a hand-held, standalone unit.

- ii. **Ground Segment:** The ground segment consists of gateway control centers (GCCs), gateway Earth stations (GESs), and the network control center (NCC). The GCC provides switching capabilities to link mobile SCs with terrestrial-based customer systems via standard communications modes. GESs link the ground segment with the space segment. GESs mainly track and monitor satellites based on orbital information from the GCC and transmit to and receive from satellites, the GCC, or the NCC. The NCC is responsible for managing the Orbcomm network elements and the gateways through telemetry monitoring, system commanding, and mission system analysis.
- iii. **Space Segment:** Orbcomm satellites are used to complete the link between the SCs and the switching capability at the NCC or GCC.

## 5.2 Orbcomm Space Segment

The Orbcomm space segment consists of a LEO satellite constellation, which at maximum capacity has up to 47 satellites in 7 orbital planes A–G, as illustrated in Figure 8. Planes A, B, and C are inclined at  $45^\circ$  to the equator and each contains 8 satellites in a circular orbit at an altitude of approximately 815 km. Plane D, also inclined at  $45^\circ$ , contains 7 satellites in a circular orbit at an altitude of 815 km. Plane E is inclined at  $0^\circ$  and contains 7 satellites in a circular orbit at an altitude of 975 km. Plane F is inclined at  $70^\circ$  and contains 2 satellites in a near-polar circular orbit at an altitude of 740 km. Plane G is inclined at  $108^\circ$  and contains 2 satellites in a near-polar elliptical orbit at an altitude varying between 785 km and 875 km.

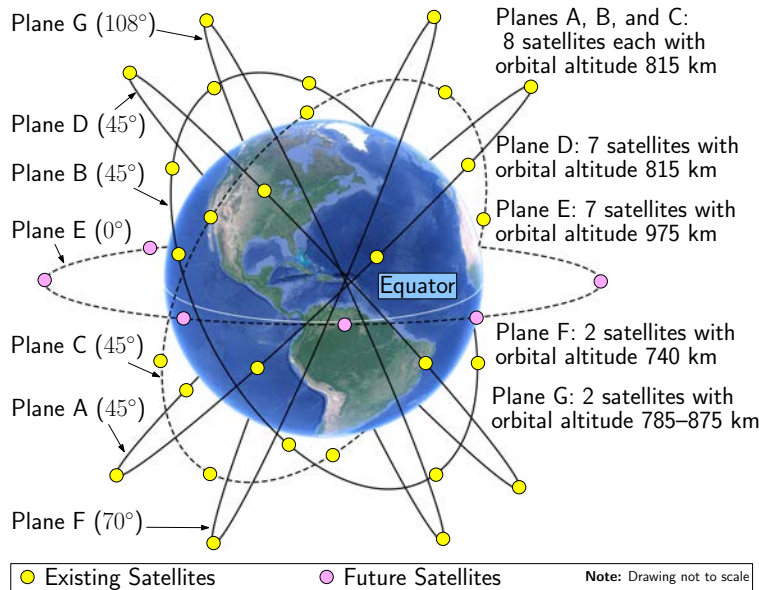


Figure 8: Orbcomm LEO satellite constellation.

### 5.3 Orbcomm Downlink Signals

The LEO receiver draws pseudorange rate observables from Orbcomm LEO signals on the downlink channel. Satellite radio frequency downlinks to SCs and GESs are within the 137–138 MHz VHF band. The downlink channels include 12 channels for transmitting to the SCs and one gateway channel, which is reserved for transmitting to the GESs. Each satellite transmits to the SCs on one of the 12 subscriber downlink channels through a frequency-sharing scheme that provides four-fold channel reuse. The Orbcomm satellites have a subscriber transmitter that provides a continuous 4800 bits-per-second (bps) stream of packet data using symmetric differential-quadrature phase shift keying (SD-QPSK). Each satellite also has multiple subscriber receivers that receive short bursts from the SCs at 2400 bps.

### 5.4 Orbcomm Receiver Design

Extracting Doppler measurements from QPSK signals transmitted by LEO satellites can be achieved through carrier synchronization, a topic well discussed in the signal processing literature [74, 75]. However, since these signals are being used opportunistically, one cannot assume that the receiver and satellites' clocks are synchronized. Therefore, the receiver's and satellite transmitters' clock drifts must be accounted for. The methods proposed in the literature on Doppler positioning with LEO satellites either assume no clock drifts or assume round-trip-type measurements [76, 77]. In contrast to these assumptions, an extended Kalman filter (EKF) can be employed to simultaneously estimate the receiver's position and the difference between the receiver's and each of the LEO satellites' clock drifts [10].

Next, a receiver architecture to produce Doppler measurements from LEO satellites transmitting direct QPSK signals is presented [10]. Throughout this section, it is assumed that the LEO satellite signals are propagating in an additive white complex Gaussian channel with a total power spectral density  $N_0$ .

The receiver simultaneously samples the bandwidth containing all LEO satellite downlink channels with a sampling period  $T$ . The received signal may be modeled

$$r(i) = \sum_{l=1}^L s_l(i) + n(i), \quad i = 0, 1, \dots,$$

where  $n(i) \triangleq n_I(i) + jn_Q(i)$ ,  $n_I$  and  $n_Q$  are modeled as zero-mean white Gaussian noise with variance  $\frac{N_0}{2T}$ , and

$$s_l(i) \triangleq \sqrt{C_l} a_l(i) \exp \{j2\pi [f_{D,l}(i) + f_{IF,l}] iT + j\theta_l(i)\},$$

where  $C_l$  is the received signal power on the  $l$ -th channel,  $a_l \triangleq \exp [j(\frac{u\pi}{2} + \frac{\pi}{4})]$  for  $u \in \{0, 1, 2, 3\}$  is the transmitted QPSK symbol on the  $l$ -th channel,  $f_{D,l}$  is the Doppler shift in the  $l$ -th channel,  $f_{IF,l}$  is the  $l$ -th channel intermediate frequency, and  $\theta_l$  is the  $l$ -th channel carrier phase shift. The time argument  $i$  implies that the corresponding quantity is evaluated at time  $t_i \triangleq t_0 + iT$  for some initial time  $t_0$ . The QPSK symbol period is  $T_{\text{symp}}$ , which is

related to the sampling period through  $T_{\text{symp}} = MT$ , where  $M$  is a large integer. It is assumed that the Doppler and carrier phase shifts are constant over  $T_{\text{symp}}$ . The signal in the  $l$ -th channel may be retrieved by mixing  $r(i)$  with the corresponding intermediate frequency and passing the resulting signal through a low-pass filter (LPF) with bandwidth  $B_l > \frac{2}{T_{\text{symp}}}$ , yielding

$$r_l(i) = \sqrt{C_l} a_l(k) \exp[j2\pi f_{D,l}(k) iT + j\theta_l(k)] + n_l(i), \quad i=0, 1, \dots,$$

where  $k \triangleq \lfloor \frac{i}{M} \rfloor$ ,  $n_l(i) \triangleq n_{I,l}(i) + jn_{Q,l}(i)$ , and  $n_{I,l}$  and  $n_{Q,l}$  are zero-mean white Gaussian noise with variance  $\frac{N_0 B_l}{2}$ . The time argument  $k$  implies that the corresponding quantity is evaluated at time  $t_k \triangleq t_0 + kT_{\text{symp}}$ . The LPFs' bandwidths  $\{B_l\}_{l=1}^L$  are chosen to be large enough to account for the Doppler shift. For Orbcomm LEO satellites, this shift can be between -3 kHz and 3 kHz.

The navigation receiver employs independent phase-locked loops (PLLs) to track the LEO satellite signal on each of the  $L$  channels. The Doppler shifts produced by the PLLs are then passed to the navigation filter, which can be an EKF or a weighted nonlinear least-squares (WNLS) estimator, as shown in Figure 9(a). Each tracking loop is a feedback loop that consists of an integrate and dump (I&D) filter, a phase discriminator, a loop filter, and a numerically controlled oscillator (NCO), as shown in Figure 9(b).

Denote  $\hat{\theta}_l(k)$  to be the current phase estimate maintained by the  $l$ -th channel's NCO and  $\hat{f}_{D,l}(k)$  to be the current Doppler shift estimate maintained by the PLL. Then, between time-steps  $k$  and  $k+1$ ,  $M$  samples of  $r_l(i)$  are mixed with the estimated residual carrier wave due to Doppler and coherently summed over  $T_{\text{symp}}$  yielding

$$\begin{aligned} \hat{s}_l(k+1) &= \frac{1}{M} \sum_{i=i_0}^{i_0+M-1} r_l(i) \exp \left[ j2\pi \hat{f}_{D,l}(k) iT + j\hat{\theta}_l(k) \right] \\ &\approx \sqrt{C_l} a_l(k+1) \exp [j\Delta\theta_l(k+1)] + \hat{n}_l(k), \end{aligned}$$

where  $\Delta\theta_l(k+1)$  is the phase error at time-step  $k+1$ ,  $\hat{n}_l(k) \triangleq \hat{n}_{I,l}(k) + j\hat{n}_{Q,l}(k)$ , and  $\hat{n}_{I,l}$  and  $\hat{n}_{Q,l}$  are zero-mean white Gaussian noise with variance  $\frac{N_0}{2T_{\text{symp}}}$ . Note that  $\hat{\theta}_l$  is updated as

$$\hat{\theta}_l(k+1) = \hat{\theta}_l(k) + 2\pi \hat{f}_{D,l}(k) MT, \quad \hat{\theta}_l(0) \equiv 0.$$

Given  $\hat{s}_l(k+1)$ , the phase error  $\Delta\theta_l(k+1)$  can be obtained using a QPSK phase discriminator. For instance, the maximum-likelihood discriminator is given by

$$\Delta\theta_l(k) = \frac{1}{\sqrt{C_l}} \{Q_l(k) \tanh [I_l(k)] - I_l(k) \tanh [Q_l(k)]\},$$

where  $I_l(k)$  and  $Q_l(k)$  are the real and imaginary parts of  $\hat{s}_l(k)$ , respectively, and  $\tanh$  is the hyperbolic tangent function [78].

The phase error at time-step  $k+1$  is then passed through the loop filter, which is a first-order filter with a continuous-time transfer function  $F(s) = \frac{2\zeta\omega_n s + \omega_n^2}{s}$ , where  $\zeta \equiv \frac{1}{\sqrt{2}}$

is the damping ratio and  $\omega_n$  is the undamped natural frequency, which can be related to the PLL noise-equivalent bandwidth  $B_{n,\text{PLL}}$  by  $B_{n,\text{PLL}} = \frac{\omega_n}{8\zeta} (4\zeta^2 + 1)$ . Denote  $v_{\text{PLL},l}$  to be the output of the filter. The Doppler frequency estimate  $\hat{f}_{D,l}(k+1)$  is deduced by dividing  $v_{\text{PLL},l}(k+1)$  by  $2\pi$ .

The loop filter transfer function is discretized and realized in state-space. The measurement vector  $\mathbf{z}_{\text{leo}}$  is formed using the Doppler shift estimates tracked by each PLL according to

$$z_{\text{leo},l}(k) \triangleq c \frac{\hat{f}_{D,l}(k)}{f_{c,l}}, \quad l = 1, \dots, L, \quad k = 0, 1, \dots, \quad (13)$$

where  $\hat{f}_{D,l}$  is the measured Doppler frequency to the  $l$ -th satellite,  $f_{c,l}$  is the carrier frequency at which the  $l$ -th satellite is transmitting, and  $c$  is the speed of light.

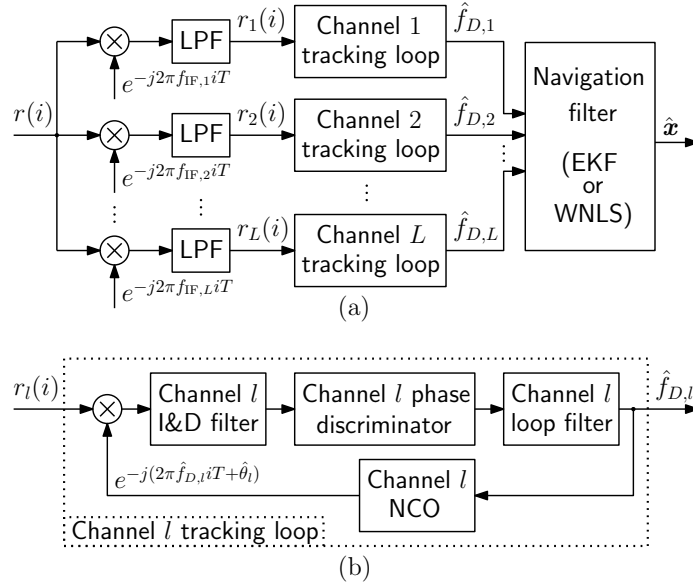


Figure 9: Navigation receiver: (a) Each channel is first extracted then fed to a tracking loop. The resulting Doppler measurements are passed to the navigation filter. (b) Tracking loop for the  $l$ -th channel.

It can be shown that the noise variance  $\sigma_{\Delta\theta,l}^2$  of the maximum-likelihood discriminator can be expressed as [78]

$$\sigma_{\Delta\theta,l}^2 = \frac{1}{\text{SNR}_l^3} \left( \frac{8}{9\text{SNR}_l^4} + \frac{20}{3\text{SNR}_l^3} + \frac{10}{3\text{SNR}_l^2} - \frac{8}{3\text{SNR}_l} + 2 \right), \quad (14)$$

where  $\text{SNR}_l = \frac{C_l T_{\text{symp}}}{N_0}$  is the signal-to-noise ratio (SNR) on the  $l$ -th channel. It can be shown that the variance of the closed-loop PLL noise is given by  $\sigma_{\text{PLL},l}^2 = 2\sigma_{\Delta\theta,l}^2 B_{n,\text{PLL}} T_{\text{symp}}$ , from which the pseudorange rate measurement noise variance can be found to be

$$\sigma_{\text{leo},l}^2 = \frac{2c^2}{f_{c,l}^2} \sigma_{\Delta\theta,l}^2 B_{n,\text{PLL}} T_{\text{symp}}. \quad (15)$$

An initial Doppler estimate is needed to initialize the tracking loops. To this end, the Fast Fourier Transform (FFT) method is used to acquire the Doppler frequency for each channel [79].

Denote  $R_{\eta,l}(K)$  to be the FFT of  $r_l(i)$  for  $i = \eta M + i_0, \dots, (\eta + 1)M + i_0 - 1$  and  $K = 0, \dots, M - 1$ , for some  $i_0 \in \mathbb{N}$  and  $\eta \in \mathbb{N}$ . Note that the argument  $K$  in  $R_{\eta,l}(K)$  maps to frequency  $f_K$  according to

$$f_K = \begin{cases} \frac{K+1-M/2}{MT}, & \text{if } M \text{ is even,} \\ \frac{K-(M-1)/2}{MT}, & \text{if } M \text{ is odd.} \end{cases}$$

Subsequently, the initial Doppler estimate is set to  $f_{\bar{K}}$ , where

$$\bar{K} = \underset{K}{\operatorname{argmax}} \sum_{\eta=1}^N |R_{\eta,l}(K)|^2,$$

and  $N$  is the number of FFT windows used for acquisition.

Figure 10 shows a snapshot of the Orbcomm spectrum, while Figure 11 shows internal signals of the receiver used to extract Doppler measurement from Orbcomm signals: (a) an estimate of the Doppler frequency, (b) the carrier phase tracking error, (c) the demodulated QPSK modulation, and (d) the QPSK symbol phase transitions. The Orbcomm receiver is part of the Multichannel Adaptive TRAnsceiver Information eXtractor (MATRIX) software-defined radio (SDR) developed by the Autonomous Systems Perception, Intelligence, and Navigation (ASPIN) Laboratory [80]. The receiver performs carrier synchronization, extracts pseudorange rate observables, and decodes Orbcomm ephemeris messages.

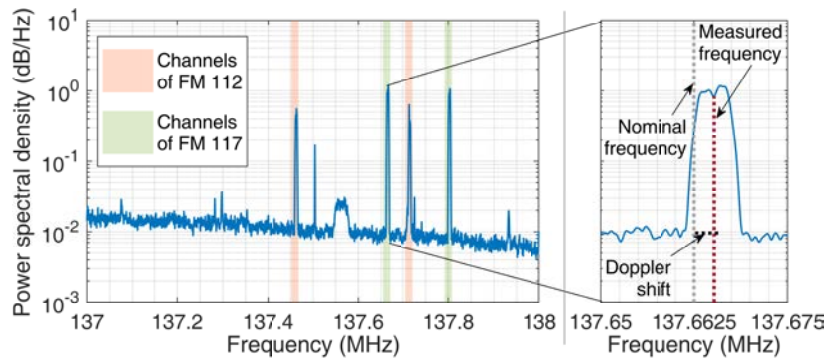


Figure 10: Snapshot of the Orbcomm spectrum.

Note that Orbcomm satellites are also equipped with a specially constructed 1-Watt ultra-high frequency (UHF) transmitter that is designed to emit a highly stable signal at 400.1 MHz. The transmitter is coupled to a UHF antenna designed to have a peak gain of approximately 2 dB. The UHF signal is used by the Orbcomm system for SC positioning. However, experimental data shows that the UHF beacon is absent. Moreover, even if the UHF beacon were present, one would need to be a paying subscriber to benefit from positioning services. Consequently, the carrier phase differential navigation framework discussed in Section 7 and the STAN framework discussed in Section 8 will only use the downlink VHF signals.

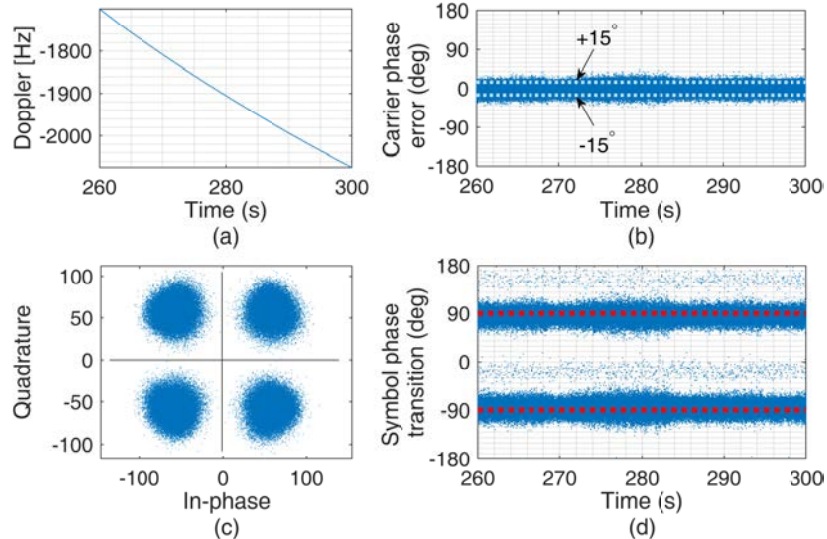


Figure 11: Outputs of Orbcomm receiver: (a) estimated Doppler, (b) carrier phase error, (c) demodulated QPSK symbols, and (d) QPSK symbol phase transitions.

## 6 Overview of Starlink LEO Satellite Constellation

This section overviews the proposed Starlink constellation according to filings, which SpaceX has made to the Federal Communications Commission (FCC) [81–83]. The currently approved Starlink satellite constellation is discussed and details are given about requested modifications.

### 6.1 Proposed Starlink Constellation

The Starlink satellite communication system is an ambitious project by SpaceX to provide the Earth with global Internet access. The Starlink system can be broken into segments consisting of satellites in LEO and very low Earth orbit (VLEO), ground control and gateway facilities, and user terminals. The current number of approved satellites is 11,943, which when launched, would more than double the amount of objects ever launched into outer space according to the United Nations Office for Outer Space Affairs (8,303 objects were listed on November 29, 2018 [84]).

SpaceX indicated in their original filing that service for licensed users will begin after the first 800 satellites are deployed. Furthermore, the FCC places milestone requirements on licensees developing satellite constellations, such as SpaceX, to launch and operate half of the proposed constellation within six-years of grant approval. Therefore, Starlink should become operational for users by 2024. Table 2 describes the most recently approved orbital configuration for the LEO and VLEO sub-constellations. It should be noted that SpaceX has requested to remove the 1,600 satellites at 1,150 km and replace them with 1,584 satellites at 550 km [83]. If approved, these satellites at 550 km would be the first deployment of satellites supported by Starlink. Fig. 12 depicts the Starlink LEO satellite constellation over Earth.

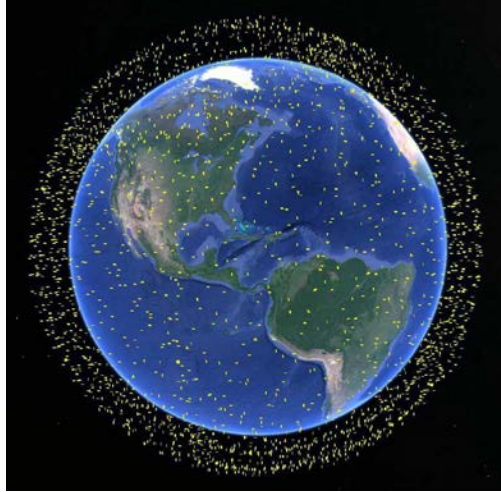


Figure 12: Visualization of proposed LEO Starlink satellites. Map data: Google Earth.

Table 2: Starlink Orbital Configuration

	LEO Constellation					VLEO Constellation		
Satellites per Altitude	1600	1600	400	375	450	2547	2478	2493
Altitude (km)	1150	1110	1130	1275	1325	354.6	340.8	335.9
Inclination ( $^{\circ}$ )	53	53.8	74	81	70	53	48	42

## 6.2 Signal Information

Users will be able to communicate with Starlink satellites once the satellites exceed a  $35^{\circ}$  elevation angle. Starlink has permission to transmit in the Ku, Ka, and V-bands. User terminals will have phased array antennas with up to  $8 \times 16$  elements using half-wavelength spacing, thus antenna apertures designed for V-band communication are expected to be approximately  $20 \text{ cm}^2$ . Steered antenna beams will track satellites to aid communication links between user terminals and LEO satellites. Additionally, downlink V-band beacon signals using between 1 and 10 MHz of spectrum will facilitate rapid satellite acquisition as handovers occur. Downlink signal beams will support both left- and right-hand polarizations and channel bandwidths of 50 MHz on the Ku-band and 1 GHz on the V-band.

## 7 Carrier Phase Differential Navigation with LEO Satellites Signals

Similar to carrier phase differential GNSS (CD-GNSS), one can formulate a carrier phase differential LEO (CD-LEO) framework consisting of a rover and a base receiver in an environment comprising  $L$  visible LEO satellites. This section formulates the CD-LEO framework [67].

## 7.1 Framework Formulation

The base receiver (B), is assumed to have knowledge of its own position state, e.g., a stationary terrestrial receiver deployed at a surveyed location or a high-flying aerial vehicle with access to GNSS. The rover (R) does not have knowledge of its position. The base communicates its own position and carrier phase observables with the rover. The LEO satellites' positions are known through the TLE files and orbit determination software, or by decoding the transmitted ephemeris, if any. Figure 13 illustrates the base/rover CD-LEO framework. Note that one could have switched the base and the rover in Figure 13 (i.e., the base being stationary and the rover being mobile), which is customary in CD-GNSS.

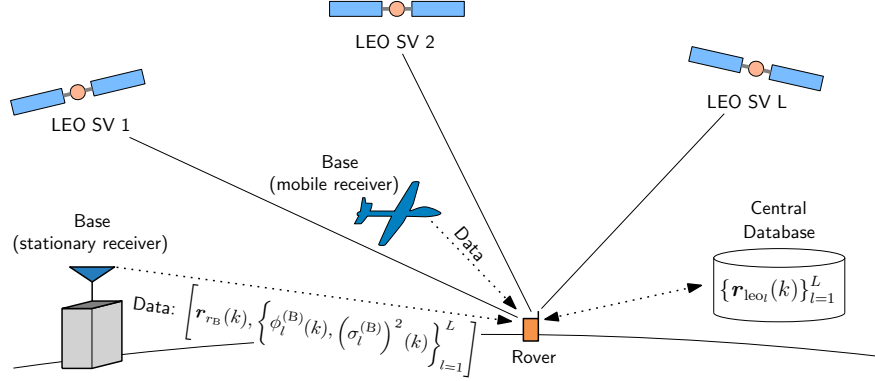


Figure 13: Base/rover CD-LEO framework. The base, which can be a stationary receiver or a high-flying aerial vehicle with complete knowledge of its position, shares its LEO carrier phase observables with a navigating receiver, i.e., the rover. The rover has no knowledge of its position and is using its LEO carrier phase observables as well as the ones shared by the base to estimate its own position.

In what follows, the objective is to estimate the rover's position, which will be achieved by double-differencing the measurements (6). Without loss of generality, let the measurements to the first LEO satellite be taken as references to form the single difference

$$\phi_{l,1}^{(i)}(k) \triangleq \phi_l^{(i)}(k) - \phi_1^{(i)}(k).$$

Subsequently, define the double difference between R and B as

$$\begin{aligned} \phi_{l,1}^{(R,B)}(k) &\triangleq \phi_{l,1}^{(R)}(k) - \phi_{l,1}^{(B)}(k) + \|\mathbf{r}_{r_B} - \mathbf{r}_{leo_l}(k)\|_2 - \|\mathbf{r}_{r_B} - \mathbf{r}_{leo_1}(k)\|_2 \\ &\triangleq h_{l,1}^{(R)}(k) + A_{l,1}^{(R,B)} + c\Delta_{iono,l,1}^{(R,B)}(k) + c\Delta_{trop,l,1}^{(R,B)}(k) + v_{l,1}^{(R,B)}(k), \end{aligned} \quad (16)$$

where  $l = 1, \dots, L$ , and

$$\begin{aligned} h_{l,1}^{(R)}(k) &\triangleq \|\mathbf{r}_{r_R} - \mathbf{r}_{leo_l}(k)\|_2 - \|\mathbf{r}_{r_R} - \mathbf{r}_{leo_1}(k)\|_2 \\ A_{l,1}^{(R,B)} &\triangleq \lambda_l N_l^{(R)} - \lambda_l N_l^{(B)} - \lambda_1 N_1^{(R)} + \lambda_1 N_1^{(B)} \\ \Delta_{iono,l,1}^{(R,B)}(k) &\triangleq \delta t_{iono,l}^{(B)}(k) - \delta t_{iono,l}^{(R)}(k) - \delta t_{iono,1}^{(B)}(k) + \delta t_{iono,1}^{(R)}(k) \\ \Delta_{trop,l,1}^{(R,B)}(k) &\triangleq \delta t_{trop,l}^{(R)}(k) - \delta t_{trop,l}^{(B)}(k) - \delta t_{trop,1}^{(R)}(k) + \delta t_{trop,1}^{(B)}(k) \\ v_{l,1}^{(R,B)}(k) &\triangleq v_l^{(R)}(k) - v_l^{(B)}(k) - v_1^{(R)}(k) + v_1^{(B)}(k). \end{aligned}$$

Note that since  $\lambda_i$  is not necessarily equal to  $\lambda_1$ , then  $A_{i,1}^{(R,B)}$  cannot necessarily be expressed as  $\lambda_i M$ , where  $M$  is an integer. Therefore,  $A_{i,1}^{(R,B)}$  is hereafter considered as a real constant parameter. Moreover, the CD-LEO framework will assume complete knowledge of the base's position (cf. (16)). This assumption implies that one expects a mobile base and a static base to yield the same positioning performance. Define the vector of measurements

$$\boldsymbol{\phi}(k) \triangleq \mathbf{h}_R(k) + \mathbf{A} + c\boldsymbol{\Delta}_{\text{iono}}(k) + c\boldsymbol{\Delta}_{\text{trop}}(k) + \mathbf{v}(k),$$

where

$$\begin{aligned} \boldsymbol{\phi}(k) &\triangleq \left[ \phi_{2,1}^{(R,B)}(k), \dots, \phi_{L,1}^{(R,B)}(k) \right]^\top \\ \mathbf{h}_R(k) &\triangleq \left[ h_{2,1}^{(R)}(k), \dots, h_{L,1}^{(R)}(k) \right]^\top \\ \mathbf{A} &\triangleq \left[ A_{2,1}^{(R,B)}, \dots, A_{L,1}^{(R,B)} \right]^\top \\ \boldsymbol{\Delta}_{\text{iono}}(k) &\triangleq \left[ \Delta_{\text{iono},2,1}^{(R,B)}(k), \dots, \Delta_{\text{iono},L,1}^{(R,B)}(k) \right]^\top \\ \boldsymbol{\Delta}_{\text{trop}}(k) &\triangleq \left[ \Delta_{\text{trop},2,1}^{(R,B)}(k), \dots, \Delta_{\text{trop},L,1}^{(R,B)}(k) \right]^\top \\ \mathbf{v}(k) &\triangleq \left[ v_{2,1}^{(R,B)}(k), \dots, v_{L,1}^{(R,B)}(k) \right]^\top, \end{aligned}$$

where  $\mathbf{v}(k)$  has a covariance  $\mathbf{R}_{R,B}(k)$  which can be readily shown to be

$$\mathbf{R}_{R,B}(k) = \mathbf{R}^{(1)}(k) + \left\{ \left[ \sigma_1^{(R)}(k) \right]^2 + \left[ \sigma_1^{(B)}(k) \right]^2 \right\} \boldsymbol{\Xi},$$

where

$$\mathbf{R}^{(1)}(k) \triangleq \text{diag} \left\{ \left[ \sigma_2^{(R)}(k) \right]^2 + \left[ \sigma_2^{(B)}(k) \right]^2, \dots, \left[ \sigma_L^{(R)}(k) \right]^2 + \left[ \sigma_L^{(B)}(k) \right]^2 \right\}$$

and  $\boldsymbol{\Xi}$  is a matrix of ones.

## 7.2 Batch Navigation Solution

The vector  $\mathbf{A}$  is unknown and has to be solved for along with the rover's position. Using only one set of carrier phase measurements with no *a priori* knowledge on the rover's position results in an underdetermined system:  $(L + 2)$  unknowns with only  $(L - 1)$  measurements. Therefore, when no *a priori* information on the position of the rover is known, the rover could remain stationary for a period of time such that enough variation in satellite geometry is observed. Subsequently, the rover uses measurements collected at different times in a batch estimator, resulting in an overdetermined system [68]. Denote  $K$  to be the number of time-steps in which carrier phase measurements are collected to be processed in a batch. Then, the total number of measurements will be  $K \times (L - 1)$  while the total number of unknowns will remain  $L + 2$ . Note that for  $L \geq 2$ , the resulting system is overdetermined for  $K \geq 4$ .

Define the collection of measurements from time-step 0 to  $K - 1$  as

$$\Phi^K \triangleq [\phi^\top(0), \dots, \phi^\top(K-1)]^\top,$$

which can be expressed as

$$\begin{aligned} \Phi^K &= \mathbf{h}^K[\mathbf{r}_{r_R}] + \bar{\mathbf{I}}^K \mathbf{A} + c\Delta_{\text{iono}}^K + c\Delta_{\text{trop}}^K + \mathbf{v}^K, \tag{17} \\ \mathbf{h}^K[\mathbf{r}_{r_R}] &\triangleq \begin{bmatrix} \mathbf{h}_R(0) \\ \vdots \\ \mathbf{h}_R(K-1) \end{bmatrix}, \quad \bar{\mathbf{I}}^K \triangleq \begin{bmatrix} \mathbf{I}_{(L-1) \times (L-1)} \\ \vdots \\ \mathbf{I}_{(L-1) \times (L-1)} \end{bmatrix}, \\ \Delta_{\text{iono}}^K &\triangleq \begin{bmatrix} \Delta_{\text{iono}}(0) \\ \vdots \\ \Delta_{\text{iono}}(K-1) \end{bmatrix}, \quad \Delta_{\text{trop}}^K \triangleq \begin{bmatrix} \Delta_{\text{trop}}(0) \\ \vdots \\ \Delta_{\text{trop}}(K-1) \end{bmatrix}, \quad \mathbf{v}^K \triangleq \begin{bmatrix} \mathbf{v}(0) \\ \vdots \\ \mathbf{v}(K-1) \end{bmatrix}, \end{aligned}$$

where  $\mathbf{v}^K$  is the measurement noise with covariance  $\mathbf{R}^K \triangleq \text{diag}[\mathbf{R}_{R,B}(0), \dots, \mathbf{R}_{R,B}(K-1)]$ . Note that the measurements in (17) contain the ionospheric and tropospheric delays, which can be estimated as discussed in Subsection 4.3. Let  $\hat{\Delta}_{\text{iono}}^K$  and  $\hat{\Delta}_{\text{trop}}^K$  denote the estimates of  $\Delta_{\text{iono}}^K$  and  $\Delta_{\text{trop}}^K$ , respectively, with the associated estimation errors

$$\tilde{\Delta}_{\text{iono}}^K \triangleq \Delta_{\text{iono}}^K - \hat{\Delta}_{\text{iono}}^K, \quad \tilde{\Delta}_{\text{trop}}^K \triangleq \Delta_{\text{trop}}^K - \hat{\Delta}_{\text{trop}}^K.$$

Subsequently, define the ionospheric delay-free and tropospheric delay-free measurements

$$\begin{aligned} \bar{\Phi}^K &\triangleq \Phi^K - c \left( \hat{\Delta}_{\text{iono}}^K + \hat{\Delta}_{\text{trop}}^K \right), \\ &= \mathbf{h}^K[\mathbf{r}_{r_R}] + \bar{\mathbf{I}}^K \mathbf{A} + \bar{\mathbf{v}}^K, \end{aligned} \tag{18}$$

where  $\bar{\mathbf{v}}^K = \mathbf{v}^K + c\tilde{\Delta}_{\text{iono}}^K + c\tilde{\Delta}_{\text{trop}}^K$  is the overall measurement noise with covariance

$$\bar{\mathbf{R}}^K = \mathbf{R}^K + \sigma_{\text{iono,trop}}^2 \mathbf{I}_{K(L-1) \times K(L-1)},$$

and  $\sigma_{\text{iono,trop}}^2$  is a tuning parameter determined empirically. A WNLS estimator with a weighting matrix  $(\bar{\mathbf{R}}^K)^{-1}$  can be used to estimate  $\mathbf{r}_{r_R}$  along with  $\mathbf{A}$ .

## 8 STAN: Simultaneous Tracking and Navigation with LEO Satellite Signals

To exploit LEO satellite signals for navigation, their states must be known. Unlike GNSS satellites that periodically transmit accurate information about their positions and clock errors, such information about LEO satellites may be unavailable. The STAN framework addresses this by extracting pseudorange and Doppler measurements from LEO satellite to aid the vehicle's INS, while simultaneously tracking the LEO satellites. The STAN framework employs an EKF to simultaneously estimate the vehicle's states with the LEO satellites'

states [6, 9, 11]. Figure 14 depicts the STAN framework. The STAN framework operates similarly to a traditional tightly-coupled GNSS-aided INS with two main differences: (i) the position and clock states of the LEO satellites are unknown to the vehicle-mounted receiver; hence, they are estimated along with the states of the navigating vehicle and (ii) LEO pseudorange and Doppler measurements are used to aid the INS instead of GNSS pseudoranges. The EKF state vector, state dynamics model, receiver’s measurement model, and the EKF prediction and measurement update are discussed next. To avoid issues of unobservability or poor estimability, certain information about the navigating vehicle’s states and/or the LEO satellite states must be known *a priori* as discussed in [15, 45, 53, 85–87].

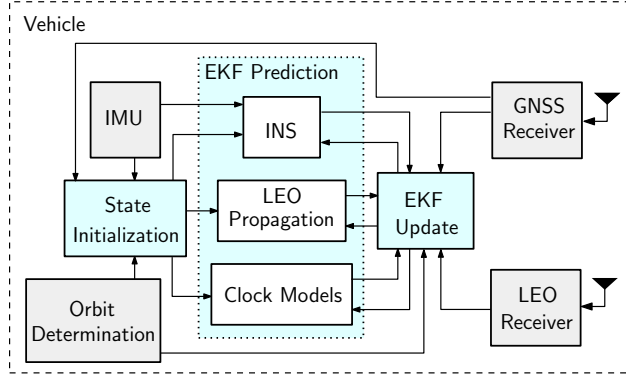


Figure 14: LEO-aided INS STAN framework.

## 8.1 EKF State Vector and Dynamics Model

### 8.1.1 EKF State Vector

The EKF state vector is given by

$$\mathbf{x} = [\mathbf{x}_r^\top, \mathbf{x}_{\text{leo}_1}^\top, \dots, \mathbf{x}_{\text{leo}_L}^\top]^\top$$

$$\mathbf{x}_r = \left[ \begin{matrix} {}^B_G \bar{\mathbf{q}}^\top, \mathbf{r}_r^\top, \dot{\mathbf{r}}_r^\top, \mathbf{b}_g^\top, \mathbf{b}_a^\top, c\delta t_r, c\dot{\delta} t_r \end{matrix} \right]^\top$$

$$\mathbf{x}_{\text{leo}_l} = \left[ \begin{matrix} \mathbf{r}_{\text{leo}_l}^\top, \dot{\mathbf{r}}_{\text{leo}_l}^\top, c\delta t_{\text{leo}_l}, c\dot{\delta} t_{\text{leo}_l} \end{matrix} \right]^\top,$$

where  $\mathbf{x}_r$  is the state vector of the vehicle-mounted inertial measurement unit (IMU) and receiver which consists of  ${}^B_G \bar{\mathbf{q}}$ , which is a four-dimensional (4-D) unit quaternion representing the orientation of a body frame  $B$  fixed at the IMU with respect to a global frame  $G$ ,  $\mathbf{r}_r$  and  $\dot{\mathbf{r}}_r$  are the 3-D position and velocity of the IMU, and  $\mathbf{b}_g$  and  $\mathbf{b}_a$  are 3-D biases of the IMU’s gyroscopes and accelerometers, respectively. The vector  $\mathbf{x}_{\text{leo}_l}$  are the states of the  $l$ -th LEO satellite, which consists of the LEO satellite position  $\mathbf{r}_{\text{leo}_l}$  and velocity  $\dot{\mathbf{r}}_{\text{leo}_l}$  and the LEO satellite clock bias  $c\delta t_{\text{leo}_l}$  and drift  $c\dot{\delta} t_{\text{leo}_l}$ , where  $l = 1, \dots, L$ , with  $L$  being the total number of LEO satellites visible to the receiver.

### 8.1.2 Vehicle Kinematics Model

The vehicle's orientation, position, and velocity are modeled to evolve in time according to INS kinematic equations driven by a 3-D rotation rate vector  ${}^B\boldsymbol{\omega}$  of the body frame and a 3-D acceleration vector  ${}^G\mathbf{a}$  in the global frame [88]. The gyroscopes' and accelerometers' biases are modeled to evolve according to

$$\mathbf{b}_g(k+1) = \mathbf{b}_g(k) + \mathbf{w}_{bg}(k) \quad (19)$$

$$\mathbf{b}_a(k+1) = \mathbf{b}_a(k) + \mathbf{w}_{ba}(k), \quad (20)$$

where  $\mathbf{w}_{bg}$  and  $\mathbf{w}_{ba}$  are process noise vectors, which are modeled as a discrete-time white noise sequences with covariances  $\mathbf{Q}_{bg}$  and  $\mathbf{Q}_{ba}$ , respectively. The vehicle-mounted receiver's clock error states are assumed to evolve in time according to

$$\mathbf{x}_{\text{clk}_r}(k+1) = \mathbf{F}_{\text{clk}} \mathbf{x}_{\text{clk}_r}(k) + \mathbf{w}_{\text{clk}_r}(k), \quad (21)$$

$$\mathbf{x}_{\text{clk}_r} \triangleq \begin{bmatrix} c\delta t_r & c\dot{\delta} t_r \end{bmatrix}^T, \quad \mathbf{F}_{\text{clk}} = \begin{bmatrix} 1 & T \\ 0 & 1 \end{bmatrix},$$

where  $\mathbf{w}_{\text{clk}_r}$  is the process noise, which is modeled as a discrete-time white noise sequence with covariance

$$\mathbf{Q}_{\text{clk}_r} = \begin{bmatrix} S_{\tilde{w}_{\delta t_r}} T + S_{\tilde{w}_{\dot{\delta} t_r}} \frac{T^3}{3} & S_{\tilde{w}_{\delta t_r}} \frac{T^2}{2} \\ S_{\tilde{w}_{\dot{\delta} t_r}} \frac{T^2}{2} & S_{\tilde{w}_{\dot{\delta} t_r}} T \end{bmatrix}, \quad (22)$$

and  $T$  is the constant sampling interval. The terms  $S_{\tilde{w}_{\delta t_r}}$  and  $S_{\tilde{w}_{\dot{\delta} t_r}}$  are the clock bias and drift process noise power spectra, respectively, which can be related to the power-law coefficients,  $\{h_{\alpha,r}\}_{\alpha=-2}^2$ , which have been shown through laboratory experiments to characterize the power spectral density of the fractional frequency deviation of an oscillator from nominal frequency according to  $S_{\tilde{w}_{\delta t_r}} \approx \frac{h_{0,r}}{2}$  and  $S_{\tilde{w}_{\dot{\delta} t_r}} \approx 2\pi^2 h_{-2,r}$  [89].

### 8.1.3 LEO Satellite Dynamics Model

The orbital dynamics of LEO satellites was discussed in Section 3. The  $l$ -th LEO satellite's clock states time evolution are modeled according to

$$\mathbf{x}_{\text{clk}_{\text{leo}_l}}(k+1) = \mathbf{F}_{\text{clk}} \mathbf{x}_{\text{clk}_{\text{leo}_l}}(k) + \mathbf{w}_{\text{clk}_{\text{leo}_l}}(k), \quad (23)$$

where  $\mathbf{w}_{\text{clk}_{\text{leo}_l}}$  is a discrete-time white noise sequence with covariance of identical structure to  $\mathbf{Q}_{\text{clk}_r}$  in (22), except that  $S_{\tilde{w}_{\delta t_r}}$  and  $S_{\tilde{w}_{\dot{\delta} t_r}}$  are replaced with the LEO satellite clock specific spectra  $S_{\tilde{w}_{\delta t_{\text{leo},l}}}$  and  $S_{\tilde{w}_{\dot{\delta} t_{\text{leo},l}}}$ , respectively, where  $S_{\tilde{w}_{\delta t_{\text{leo},l}}} \approx \frac{h_{0,\text{leo}_l}}{2}$  and  $S_{\tilde{w}_{\dot{\delta} t_{\text{leo},l}}} \approx 2\pi^2 h_{-2,\text{leo}_l}$ . The next section discusses how these models are used in the EKF prediction.

## 8.2 IMU Measurement Model and EKF Prediction

The vehicle-mounted IMU contains a triad-gyroscope and triad-accelerometer and produces angular rate  $\boldsymbol{\omega}_{\text{imu}}$  and specific force  $\mathbf{a}_{\text{imu}}$  measurements, which are modeled as

$$\boldsymbol{\omega}_{\text{imu}}(k) = {}^B\boldsymbol{\omega}(k) + \mathbf{b}_g(k) + \mathbf{n}_g(k) \quad (24)$$

$$\mathbf{a}_{\text{imu}}(k) = \mathbf{R} \left[ \begin{smallmatrix} B \\ G \end{smallmatrix} \bar{\mathbf{q}}(k) \right] \left( {}^G \mathbf{a}(k) - {}^G \mathbf{g}(k) \right) + \mathbf{b}_a(k) + \mathbf{n}_a(k), \quad k = 1, 2, \dots, \quad (25)$$

where  $\mathbf{R} \left[ \begin{smallmatrix} B \\ G \end{smallmatrix} \bar{\mathbf{q}} \right]$  is the equivalent rotation matrix of  $\bar{\mathbf{q}}$ ;  ${}^G \mathbf{g}$  is the acceleration due to gravity in the global frame; and  $\mathbf{n}_g$  and  $\mathbf{n}_a$  are measurement noise vectors, which are modeled as white noise sequences with covariances  $\sigma_g^2 \mathbf{I}_{3 \times 3}$  and  $\sigma_a^2 \mathbf{I}_{3 \times 3}$ , respectively.

The EKF prediction produces  $\hat{\mathbf{x}}(k|j) \triangleq \mathbb{E}[\mathbf{x}(k)|\mathbf{Z}^j]$  of  $\mathbf{x}(k)$ , and an associated estimation error covariance  $\mathbf{P}_x(k|j)$ , where  $\mathbb{E}[\cdot|\cdot]$  is the conditional expectation operator,  $\mathbf{Z}^j \triangleq \{\mathbf{z}(i)\}_{i=1}^j$  are the set of measurements available up to and including time index  $j$ , and  $k > j$ . The measurements  $\mathbf{z}$  are the pseudorange, Doppler, and/or carrier phase measurements discussed in Section 2.

The IMU measurements (24) and (25) are processed through strapdown INS equations using an Earth-centered Earth-fixed (ECEF) frame as frame  $G$  to produce  ${}^B_G \hat{\mathbf{q}}(k|j)$ ,  $\hat{\mathbf{r}}_r(k|j)$ , and  $\hat{\mathbf{r}}_r(k|j)$  [53, 90]. The gyroscopes' and accelerometers' biases predictions  $\hat{\mathbf{b}}_g(k|j)$  and  $\hat{\mathbf{b}}_a(k|j)$  follow from (19) and (20), respectively. The prediction of the clock states of both the receiver and the LEO satellite transceivers follow from (21) and (23), respectively. The prediction of the LEO satellites' position and velocity is performed by linearizing and discretizing (7). Next, the measurement model and the EKF measurement update are described.

### 8.3 Receiver Measurement Model and EKF Update

The vehicle-mounted LEO receiver makes pseudorange, Doppler, and/or carrier phase measurements whose models were discussed in Section 2. The STAN framework operates in two modes: (i) a tracking mode when GNSS measurements are available and (ii) a STAN mode when GNSS signals are unavailable. In the tracking mode, the measurement vector  $\mathbf{z}$  processed by the EKF update is defined by stacking all available GNSS pseudoranges  $\rho_{\text{gnss}}$  and LEO satellite pseudorange  $\rho_{\text{leo}}$ , pseudorange rate  $\dot{\rho}_{\text{leo}}$ , and/or carrier phase  $\phi_{\text{leo}}$  measurements. The EKF update produces  $\hat{\mathbf{x}}(j|j)$  and an associated posterior estimation error covariance  $\mathbf{P}_x(j|j)$ . When GNSS measurements become unavailable, the framework switches to the STAN mode, at which point the measurement vector only consists of LEO satellite pseudorange  $\rho_{\text{leo}}$ , pseudorange rate  $\dot{\rho}_{\text{leo}}$ , and/or carrier phase  $\phi_{\text{leo}}$  measurements.

## 9 Dilution of Precision Analysis

This section analyzes the position dilution of precision (PDOP) with some existing and future LEO satellite constellations. Similar analysis can be carried out for other constellations.

First, consider the existing Orbcomm constellation. One important measure of the estimability (i.e., degree of observability) of the receiver's position is the PDOP, given by  $\text{PDOP} = \text{trace}[\mathbf{P}_r]$ , where  $\mathbf{P}_r$  corresponds to the top  $3 \times 3$  block of  $(\mathbf{H}^T \mathbf{H})^{-1}$ , where  $\mathbf{H}$  is the measurement Jacobian matrix. In the sequel, it is assumed that the receiver is equipped with an altimeter; hence, it knows its altitude. Subsequently, only the receiver's horizontal position is estimated. As a result, the PDOP now corresponds to the horizontal dilution of precision (HDOP). The PDOP of the Orbcomm constellation is analyzed for the CD-LEO

framework discussed in Section 7. Figure 15 shows  $\log_{10}[\text{PDOP}]$  for 2 and 3 Orbcomm satellites at two positions on Earth (Seattle, WA, USA, and Quito, Ecuador).



Figure 15: Logarithm of the PDOP as a function of time at two positions on Earth (Seattle, WA, USA, and Quito, Ecuador) for 2 and 3 Orbcomm satellites.

Next, the PDOP is analyzed over a total period of 2 hours, which is about the orbital period of Orbcomm LEO satellites. The 2-hour period is divided into 4 segments, 30 minutes each, starting midnight of June 27, 2019, UTC time. In each segment, the best PDOP for a batch window of 8 minutes is computed for the entire globe. The resulting heat maps of  $\log_{10}[\text{PDOP}]$  are shown in Figure 16. The heat map combining the 4 heat maps is shown in Figure 17. It can be seen from Figure 16(a)–(d) and Figure 17 that there exists substantial regions on Earth where a less than unity PDOP can be achieved for an 8-minute batch window, implying the potential for submeter-accurate positioning with Orbcomm satellites.

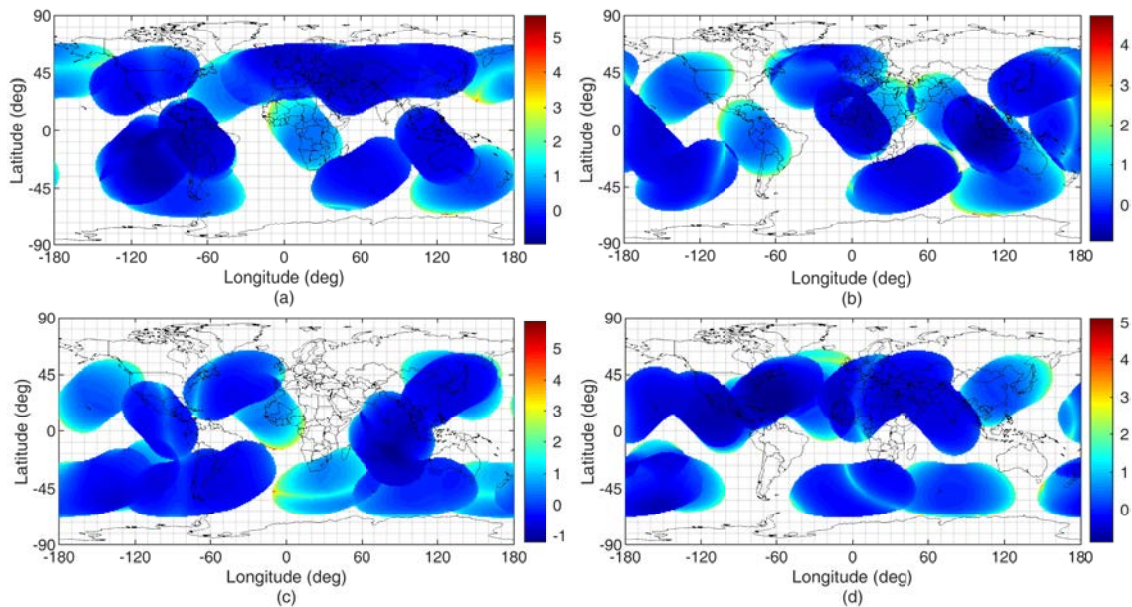


Figure 16: Heat map of  $\log_{10}[\text{PDOP}]$  for Orbcomm constellation and an 8-minute batch window. The map is computed 4 times (a)–(d) at 30 minute intervals, starting at midnight of June 27, 2019, UTC time. White regions indicate unavailability of a position solution.

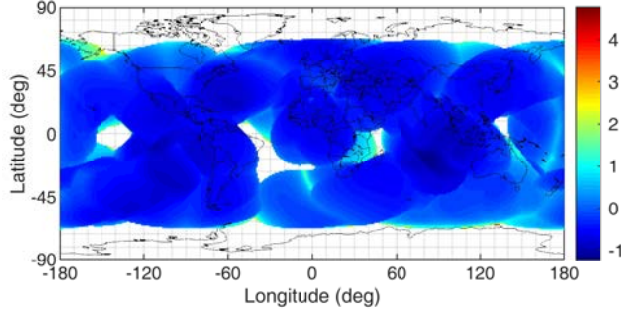


Figure 17: Heat map of  $\log_{10} [\text{PDOP}]$  for the Orbcomm constellation and an 8-minute window combined over 2 hours. White regions indicate unavailability of a position solution.

Now, consider the future Starlink constellation. Figure 18 depicts a snapshot of the upcoming Starlink constellation, while Figure 19 is a heat map of the number of visible Starlink LEO satellites above an elevation mask of 5 degrees. Figure 20 is a heat map showing the PDOP for the Starlink constellation, while Figure 21 is a heat map showing the logarithm of the Doppler position dilution of precision (DPDOP). From Figure 20, it can be seen that unlike the Orbcomm constellation, (i) an instantaneous position solution can be available anytime, anywhere on Earth and (ii) a less than unity PDOP may be observed in a substantial part of the globe.

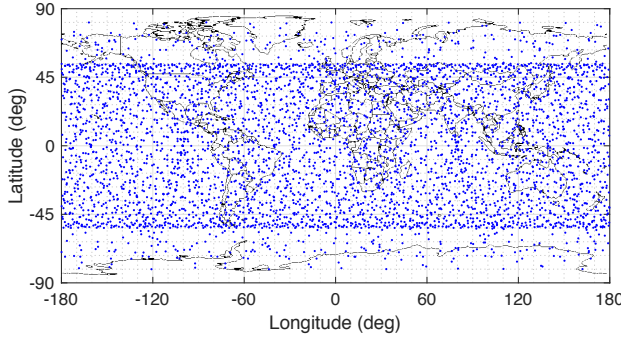


Figure 18: Snapshot of the Starlink LEO constellation.

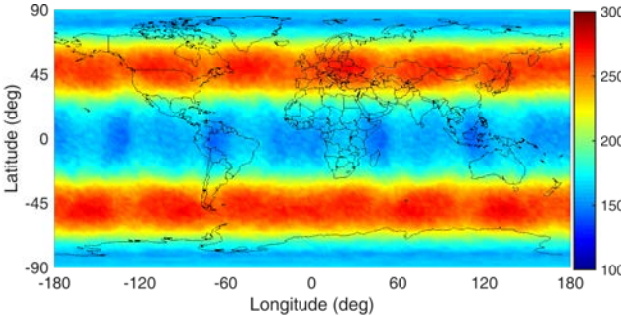


Figure 19: Heat map showing a snapshot of the number of visible Starlink LEO satellites above a 5-degree elevation mask.

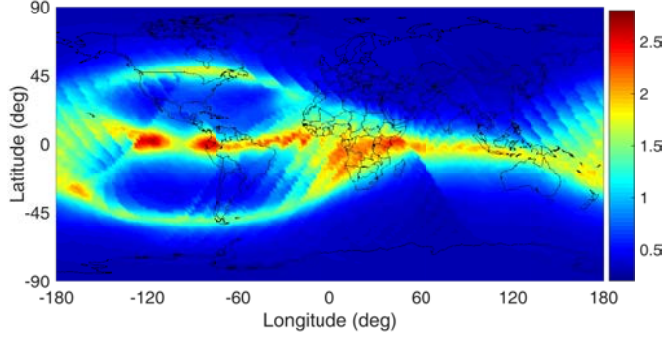


Figure 20: Heat map showing PDOP for the Starlink LEO constellation above a 5-degree elevation mask.

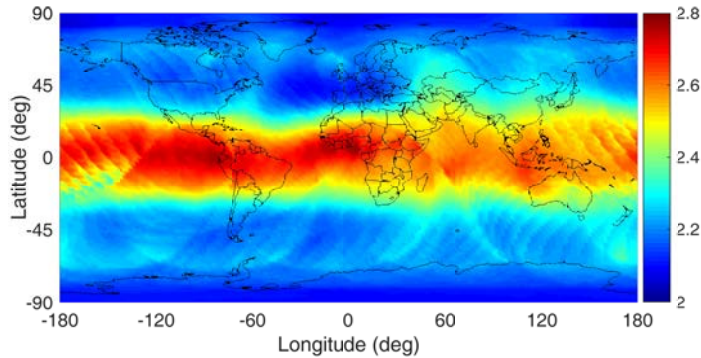


Figure 21: Heat map showing  $\log_{10}[\text{DPDOP}]$  for the Starlink LEO constellation above a 5-degree elevation mask.

## 10 Simulation Results

This section presents simulation results evaluating the navigation solution produced by (i) standalone LEO with Doppler measurements and (ii) LEO-aided INS STAN framework with pseudorange and Doppler measurements.

### 10.1 Standalone Navigation Solution with LEO Satellite Signals

This subsection presents simulation results demonstrating the navigation solution performance with Doppler measurements from LEO satellite signals [10]. To this end, a receiver was assumed to be located in Riverside, California, USA, and its position estimate was initialized around 28 km away from ground-truth. The simulated LEO satellite trajectories were generated using TLEs of 3 LEO satellite constellations: OrbcComm, Iridium, and Globalstar, with uncertainties of 10 m cross-track and 100 m along-track, emulating somewhat precise knowledge of LEO satellite orbits. The number of simulated LEO satellites  $L$  was varied between 5 and 25, in increments of 5. Note that some satellite trajectories were shifted in time in order to reach the desired number of available satellites. Doppler

measurements were generated for each satellites and were fed into an EKF, which estimated  $\mathbf{x} \triangleq [\mathbf{r}_r^\top, c\Delta\dot{\delta}t_1, \dots, c\Delta\dot{\delta}t_L]^\top$ , where  $\Delta\dot{\delta}t_l \triangleq \dot{\delta}t_r - \dot{\delta}t_{\text{leo},l}$ . For each value of  $L$ , the EKF ran for  $\Delta T = 1, 2$ , and 4 minutes. The clock drifts were simulated as uniformly distributed random numbers between  $-50$  and  $50$  m/s. The simulation SNR was chosen to be  $\text{SNR}_0 \times \sin el$ , where  $el$  is the satellite elevation angle,  $\text{SNR}_0$  is the SNR at zenith, which was set to 10 dBs, and  $\sigma_{\text{alt}}^2$  was set to  $1 \text{ m}^2$ . The elevation angle mask was set to  $10^\circ$ . The clock drift estimates in the EKF were initialized using the position prior and the first Doppler frequency measurements. The initial estimation error covariance was set to  $\mathbf{P}(0|0) \equiv \text{blkdiag}[\text{diag}[10^8, 10^8, 1], 10^3 \mathbf{I}_{L \times L}]$ . For each  $(L, \Delta T)$  pair, 100 Monte Carlo runs were performed. The final position root mean-squared errors (RMSEs) are given in Table 3.

Table 3: RMSEs (in meters) from 100 Monte Carlo runs for varying number of available LEO satellites  $L$  and positioning duration  $\Delta T$ .

$\Delta T \backslash L$	5	10	15	20	25
1 minute	168.53	100.78	74.01	55.52	37.95
2 minutes	111.25	84.12	50.03	31.34	20.27
4 minutes	28.30	27.10	20.93	17.63	11.38

## 10.2 LEO-Aided INS STAN

This subsection presents simulation results obtained with a realistic simulation environment demonstrating unmanned aerial vehicles (UAVs) navigating via the LEO-aided INS STAN framework without GNSS signals. The first subsection evaluates the achieved performance from existing LEO constellations: Globalstar, Orbcomm, and Iridium, while the second subsection evaluates the achieved performance with the future Starlink LEO constellation.

### 10.2.1 UAV Simulation with Globalstar, Orbcomm, and Iridium LEO Constellations

A UAV was equipped with (i) a tactical-grade IMU, (ii) GPS and LEO satellite receivers, and (iii) a pressure altimeter. The UAV navigated over Santa Monica, California, USA, for about 25 km in 200 seconds, during which it had access to GPS signals only for the first 100 seconds. After lift-off, the UAV made four banking turns. Ten LEO satellite trajectories were simulated. The LEO satellite orbits corresponded to the Globalstar, Orbcomm, and Iridium constellations. The UAV made pseudorange and pseudorange rate measurements to all ten LEO satellites throughout the entire trajectory. The LEO satellites' positions and velocities were initialized using TLE files and SGP4 propagation. Figure 22 shows the trajectories of the simulated LEO satellites and the UAV along with the location at which GPS signals were cut off [6].

Two navigation frameworks were implemented to estimate the UAV's trajectory: (i) the LEO-aided INS STAN framework and (ii) a traditional GPS-aided INS for comparative

analysis. Each framework had access to GPS for only the first 100 seconds. Figure 23(a)-(b) illustrate the UAV's true trajectory and those estimated by each of the two frameworks while Figure 23(c) illustrates the simulated and estimated trajectories of one of the LEO satellites, as well as the final 95-th percentile uncertainty ellipsoid (the axes denote the radial (ra) and along-track (at) directions). Table 4 summarizes the final error and position root mean squared error (RMSE) achieved by each framework after GPS cutoff.

Table 4: Simulation results with Globalstar, Orbcomm, and Iridium LEO satellites for a UAV navigating 25 km in 200 seconds (GPS signals were cut off after the first 100 seconds). These results are after GPS cutoff.

	Unaided INS	LEO-aided INS STAN
Final Error (m)	174.7	9.9
RMSE (m)	52.6	10.5

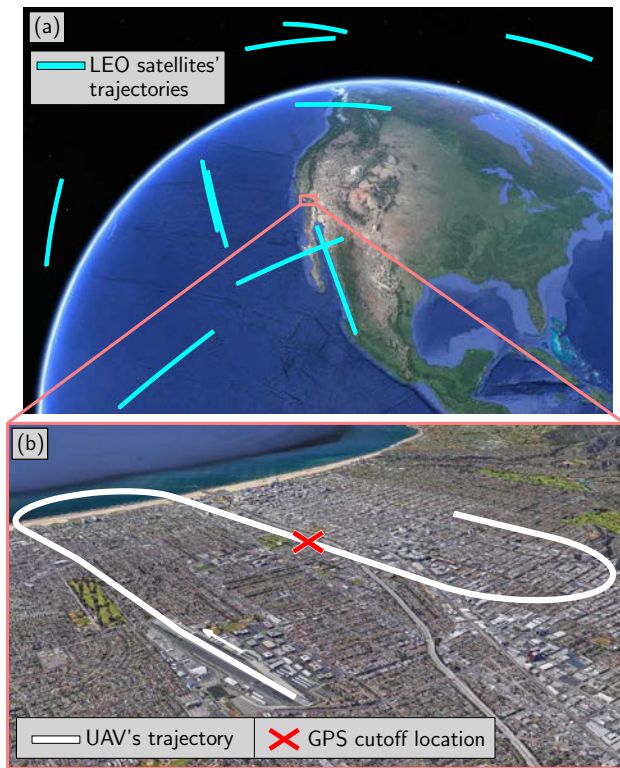


Figure 22: UAV simulation environment with the Globalstar, Orbcomm, and Iridium LEO constellations. (a) LEO satellites' trajectories. (b) UAV trajectory and GPS cutoff location. Map data: Google Earth.

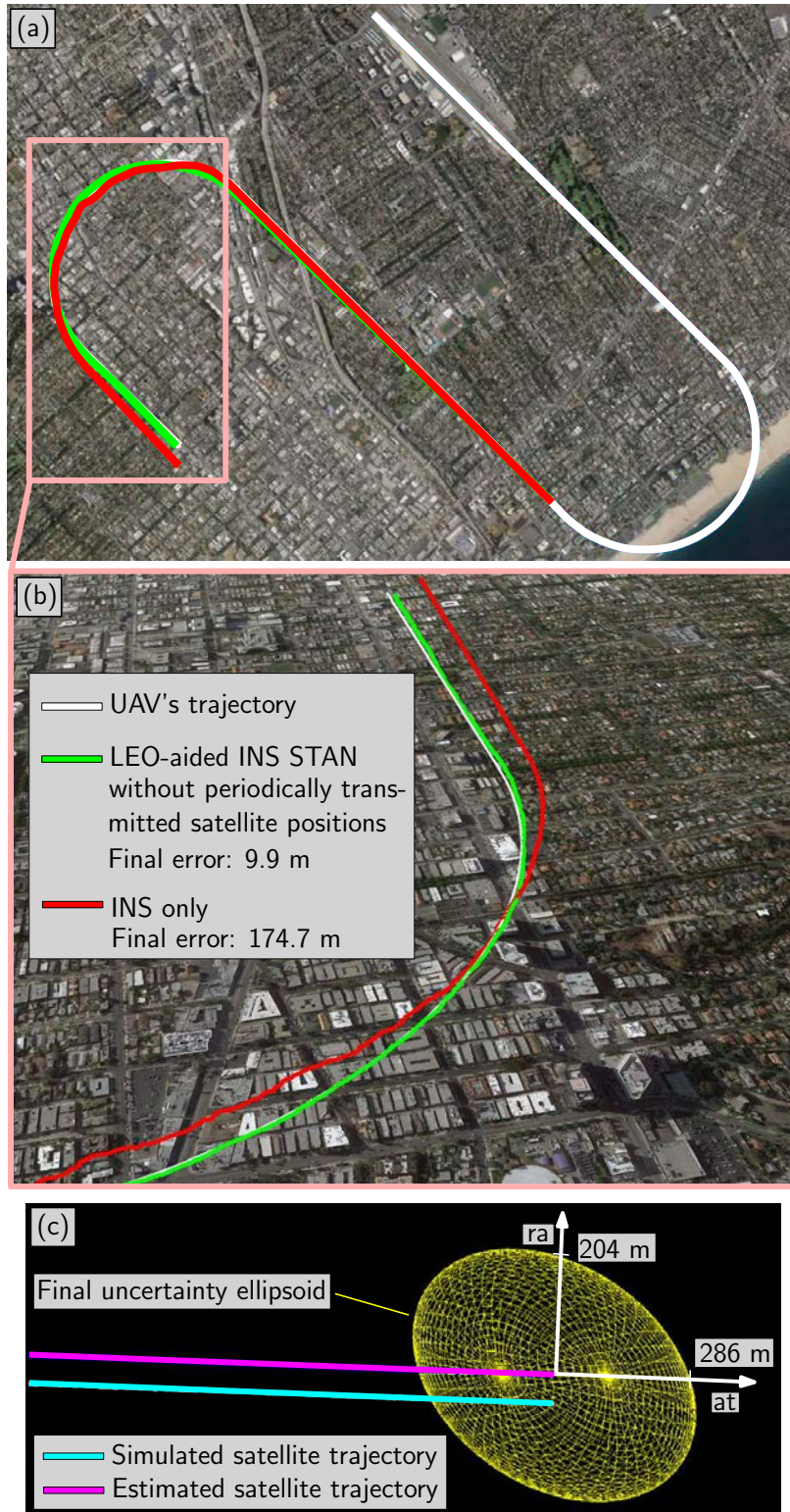


Figure 23: UAV simulation results with the Globalstar, Orbcomm, and Iridium LEO constellations. (a)-(b) UAV simulated and estimated trajectories. (c) Simulated and estimated trajectories and the final 95-th percentile uncertainty ellipsoid for one of the simulated LEO satellites. Map data: Google Earth.

## 10.2.2 UAV Simulation with the Starlink LEO Constellation with Periodically Transmitted LEO Satellite Positions

A UAV was equipped with (i) a tactical-grade IMU and (ii) GPS and LEO receivers. The UAV navigated over Santa Monica, California, USA, for about 82 km in 10 minutes, during which it had access to GPS signals only for the first 100 seconds. After lift-off, the UAV made ten banking turns. The simulated LEO satellite trajectories corresponded to the future Starlink constellation. It was assumed that the LEO satellites were equipped with GPS receivers and were periodically transmitting their estimated position every one second. There was a total of 78 LEO satellites that passed within a preset  $35^\circ$  elevation mask, with an average of 27 satellites available at any point in time. The UAV made pseudorange and pseudorange rate measurements to all LEO satellites. The LEO satellites' positions in the STAN framework were initialized using the first transmitted LEO satellite positions, which were produced by the GPS receivers onboard the LEO satellites. Figure 24 shows the trajectories of simulated LEO satellites and UAV along with the location at which GPS signals were cut off [11].

Two navigation frameworks were implemented to estimate the UAV's trajectory: (i) the LEO-aided INS STAN framework and (ii) a traditional GPS-aided INS for comparative analysis. Each framework had access to GPS for only the first 100 seconds. Figure 25(a)-(b) illustrate the UAV's true trajectory and those estimated by each of the two frameworks while Figure 25(c) illustrates the simulated and estimated trajectories of one of the LEO satellites, as well as the final 95-th percentile uncertainty ellipsoid (the axes denote the radial (ra) and along-track (at) directions). Table 5 summarizes the final error and position RMSE achieved by each framework after GPS cutoff.

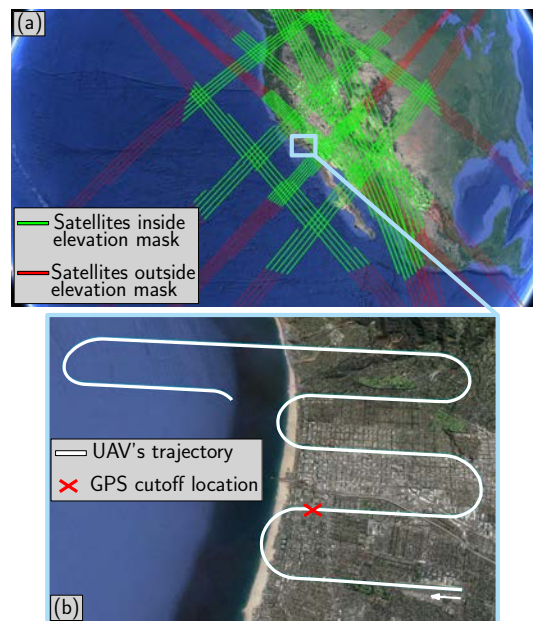


Figure 24: UAV simulation environment with the Starlink LEO constellation. (a) LEO satellites' trajectories. The elevation mask was set to 35 degrees. (b) UAV trajectory and GPS cut off location. Map data: Google Earth.

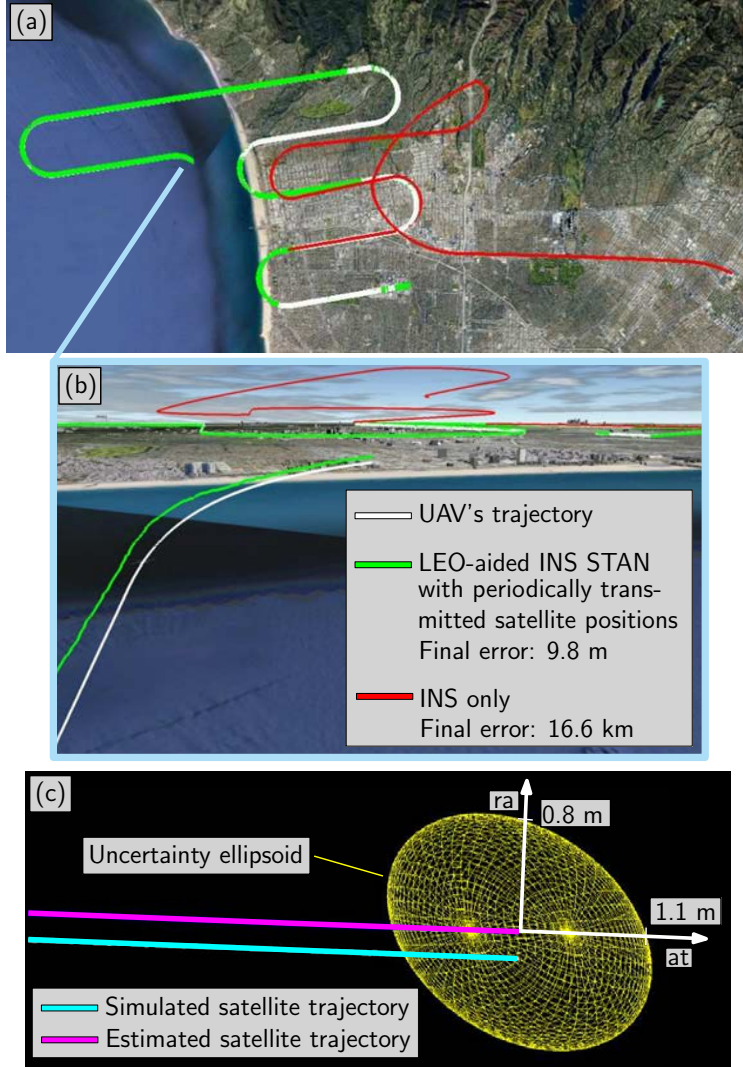


Figure 25: UAV simulation results with the Starlink LEO constellation. (a)-(b) UAV simulated and estimated trajectories. (c) Simulated and estimated trajectories and the final 95-th percentile uncertainty ellipsoid for one of the simulated LEO satellites. Map data: Google Earth.

Table 5: Simulation results with Starlink LEO satellites for a UAV navigating 82 km in 600 seconds (GPS signals were cut off after the first 100 seconds). These results are after GPS cutoff.

	Unaided INS	LEO-aided INS STAN with periodically transmitted satellite positions
Final Error (m)	16,589.0	9.8
RMSE (m)	6,864.6	10.1

# 11 Experimental Results

This section presents experimental results evaluating the navigation performance with LEO satellites. First, the standalone navigation solution with LEO Doppler measurements is evaluated. Next, the navigation solution with the CD-LEO framework using Doppler measurements is evaluated. Finally, the navigation solution with the LEO-aided INS STAN framework with Doppler measurements is evaluated on a UAV and a ground vehicle.

## 11.1 Standalone Navigation Solution with LEO Satellite Signals

An experiment was conducted to demonstrate the navigation solution performance with Doppler measurements from existing Orbcomm LEO satellites. To this end, a multipurpose low-cost VHF dipole antenna and an RTL-SDR dongle were used to sample Orbcomm signals. The samples were stored on a laptop and then processed by the MATRIX SDR. The true altitude of the antenna was used in the initial position estimate since no altimeter measurements were available. Over the course of the experiment, two Orbcomm LEO satellites were available for 60 seconds, one transmitting at 137.3125 MHz and the other at 137.25 MHz. The satellite positions and velocities were obtained using SGP 4 propagation software written in MATLAB and TLE files available online [91]. The EKF was initialized similarly to the simulation results section. The SNR was calculated using the signal-to-variation method [92]. The final  $xy$ -position error in the EKF was 358 m. The expected Doppler obtained from SGP 4 propagation is shown in Figure 26(a) along with the Doppler frequencies measured by the proposed SDR. The true receiver position, the final position estimate, and the final position uncertainty ellipse are shown in Figure 26(b).

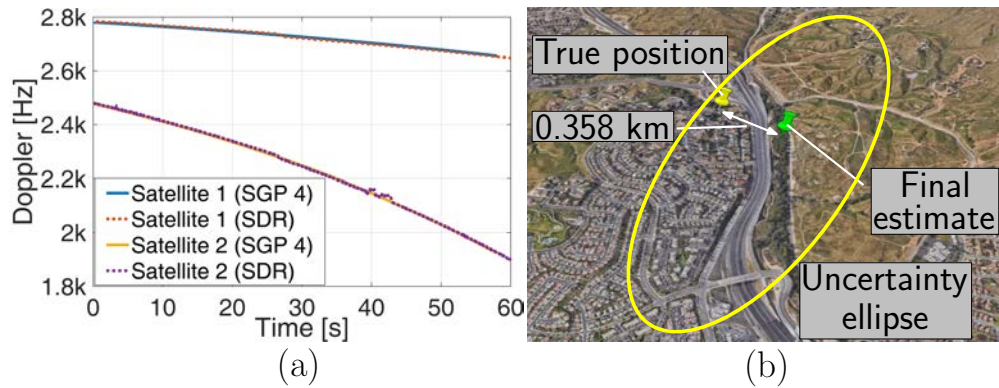


Figure 26: Experimental results showing (a) the expected and measured Doppler and (b) positioning of a stationary receiver with Doppler measurements from 2 Orbcomm LEO satellites.

It is important to note that in this experiment, the satellite positions and velocities were obtained from TLE files, which can be off by a few kilometers and tens of meters per seconds, respectively. This is one major source of error that should be considered. One way to account for this source of error is by inflating the measurement noise variance. Furthermore, it was assumed that the receiver and satellite clock drifts were constant, which is not necessarily the case. Moreover, ionospheric and tropospheric delay rates were neglected, which also

degrades the positioning performance. Despite these sources of error, the receiver was able to position itself within 360 m from its true position in 1 minute. In contrast, the simulation results presented in Subsection 10.1, considered an uncertainty of 10 m in the cross-track and 100 m in the along-track, emulating a more accurate knowledge of the satellite trajectory than in the experiments. Moreover, no model mismatches were introduced (i.e., constant clock drifts and no ionospheric or tropospheric delay rates). Under such conditions, 11 m RMSE can be achieved.

## 11.2 CD-LEO Navigation Results

In this subsection, experimental results are presented demonstrating positioning with the CD-LEO framework developed in Section 7. Only the 2-D position of the rover is estimated as its altitude may be obtained using other sensors (e.g., altimeter). In the following experiments, the altitude of the rover was obtained from its surveyed location. The noise equivalent bandwidths of the receivers' PLLs were set to  $B_{R,PLL} = B_{B,PLL} = B_{PLL} = 18$  Hz. In order to demonstrate the CD-LEO framework discussed in Section 7, the base, which was a DJI Matrice 600 UAV, was equipped with an Ettus E312 USRP, a high-end VHF antenna, and a small consumer-grade GPS antenna to discipline the on-board oscillator. The rover, which was a stationary receiver, was equipped with an Ettus E312 USRP, a custom-made VHF antenna, and a small consumer-grade GPS antenna to discipline the on-board oscillator. The receivers were tuned to a 137 MHz carrier frequency with more than 1 MHz sampling bandwidth, which covers the 137–138 MHz band allocated to Orbcomm satellites. Samples of the received signals were stored for off-line post-processing using the MATRIX SDR. The LEO carrier phase measurements were given at a rate of 4.8 kHz and were downsampled to 1 Hz. The ground-truth reference for the rover was surveyed on Google Earth, and the trajectory of the base UAV was taken from its on-board navigation system, which uses GNSS (GPS and GLONASS), an IMU, and other sensors. The experimental setup is shown in Fig. 27.

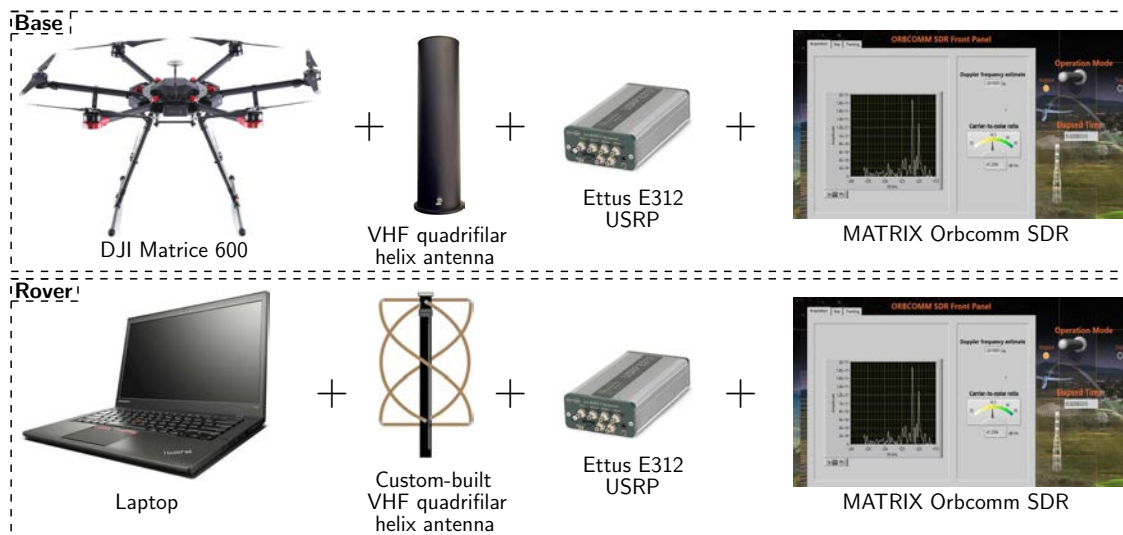


Figure 27: Base/rover experimental setup of the CD-LEO framework.

The rover waited 114 s to produce a position estimate. Over the course of the experiment, the receivers on-board the base and the rover were listening to 2 Orbcmm satellites, namely FM 108 and FM 116, whose positions were decoded from the transmitted ephemeris and interpolated at 1 Hz rate. A sky plot of the 2 Orbcmm satellites is shown in Figure 28(a). The Doppler frequency measured by the rover using the MATRIX SDR for the 2 Orbcmm satellites is shown along with the expected Doppler calculated from the TLE files in Figure 28(b). The CD-LEO measurement residual and the double-difference of the combined ionospheric and tropospheric delays calculated using the models in Subsection 4.3,  $c\hat{\Delta}_{\text{iono},1}^{(R,B)}(k) + c\hat{\Delta}_{\text{trop},1}^{(R,B)}(k)$ , are shown in Figure 27(c). It can be seen that the combined double-differenced ionospheric and tropospheric delays are negligible since the rover was within only 200 m of the base throughout the experiment. Therefore, the CD-LEO measurement residual is mainly due to measurement noise and unmodeled errors. Note that the base was mobile during the experiment and the position returned by its on-board navigation system was used as ground-truth. Consequently, any errors in the UAV's navigation solution would have reflected in the residual delays and degraded the rover's position estimate.

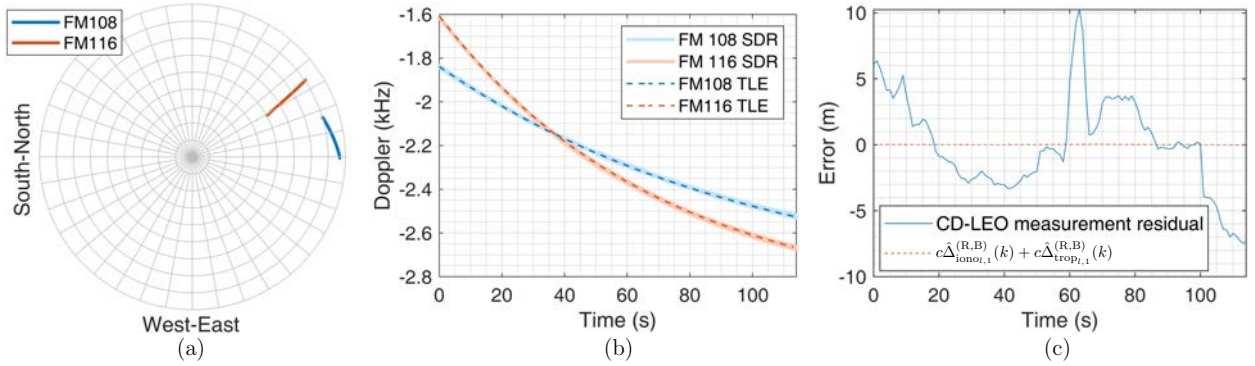


Figure 28: (a) Sky plot showing the geometry of the 2 Orbcmm satellites during the experiment. (b) The measured Doppler frequencies using the MATRIX SDR and the expected Doppler calculated from the TLE for both Orbcmm satellites. (c) CD-LEO measurement residual and combined double-differenced ionospheric and tropospheric delays.

The CD-LEO measurements were used to estimate the rover's position via the base/rover framework developed in Section 7. The satellites' trajectories, the true and estimated rover position, and the base UAV trajectory are shown in Fig. 29. The position error was found to be 11.93 m. The PDOP was found to be 29.17. Assuming a precision of  $\lambda/2$  in the CD-LEO measurements, it is found that the position error obtained in this experiment is well below the  $1 - \sigma$  bound.

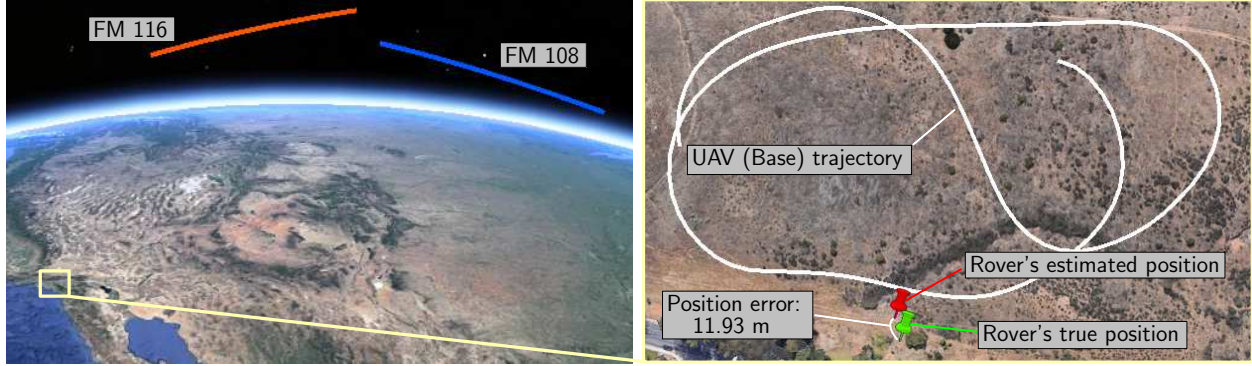


Figure 29: Trajectory of the 2 Orbcomm satellites during the experiment, trajectory of the base UAV, and the rover’s true and estimated position. Map data: Google Earth.

### 11.3 LEO-Aided INS STAN

This subsection presents navigation results via the LEO-aided INS STAN framework on ground and aerial vehicles.

#### 11.3.1 Ground Vehicle

An experiment was conducted to evaluate the performance of the LEO-aided INS STAN framework on a ground vehicle traversing a long trajectory. The experimental setup is shown in Figure 30.

The ground vehicle was driven along U.S. Interstate 5 near Irvine, California, USA, for 7,495 m in 258 seconds, during which 2 Orbcomm LEO satellites were available (FM 112 and FM 117). Figure 31(a) depicts a skyplot of the satellite trajectories over the course of the experiment. Figure 31(b) shows the Doppler measured by the MATRIX SDR and the estimated Doppler using satellite position and velocity obtained from TLE files and an SGP4 propagator for the 2 Orbcomm satellites.

Two navigation frameworks were implemented to estimate the ground vehicle’s trajectory: (i) the LEO-aided INS STAN framework and (ii) a traditional GPS-aided INS for comparative analysis. Each framework had access to GPS for only the first 30 seconds. Figure 32(a) illustrate the trajectory the 2 Orbcomm LEO satellites traversed over the course of the experiment, Figure 32(b)-(c) illustrate the ground vehicle’s true trajectory and those estimated by each of the two frameworks, and Figure 32(d) illustrates the estimated trajectories of one of the Orbcomm satellites as well as the final 95-th percentile uncertainty ellipsoid (the axes denote the radial ( $r_a$ ) and along-track ( $a_t$ ) directions).

Table 6 summarizes the final error and position RMSE achieved by each framework after GPS cutoff.

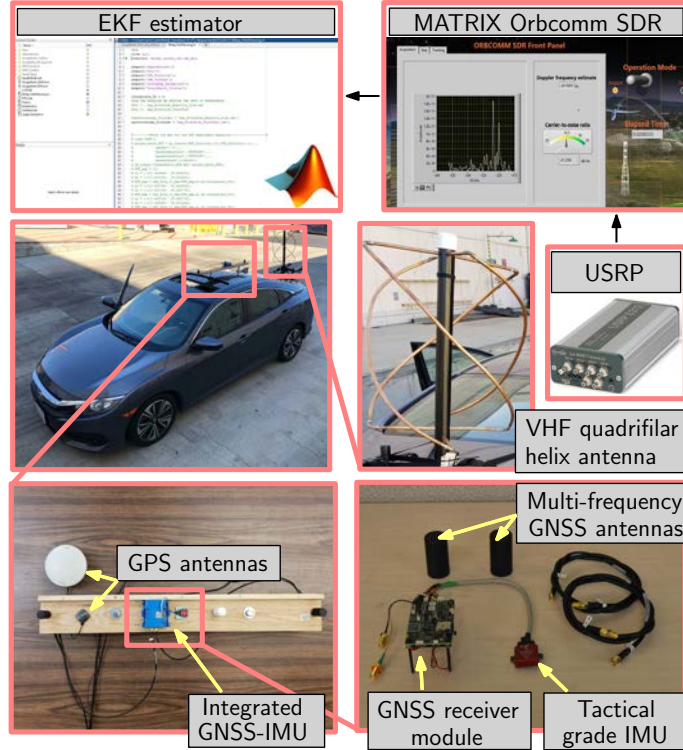


Figure 30: Hardware and software setup for the ground vehicle experiment.

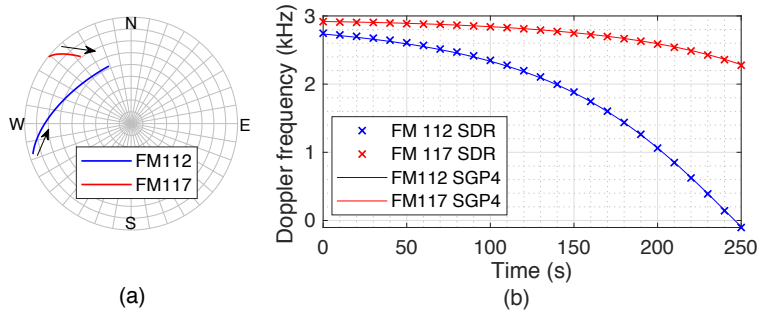


Figure 31: (a) Skyplot of the Orbcomm satellite trajectories. (b) Doppler frequency measurement produced by the MATRIX SDR and the expected Doppler according to an SGP4 propagator for the ground vehicle experiment.

Table 6: Experimental results with 2 Orbcomm LEO satellites for a ground vehicle navigating about 7.5 km in 258 seconds (GPS signals were cut off after the first 30 seconds). These results are after GPS cutoff.

	Unaided INS	LEO-aided INS STAN
Final Error (m)	3,729.4	192.3
RMSE (m)	1,419.3	416.5



Figure 32: Results of the ground vehicle experiment. (a) Orbcomm satellite trajectories. (b)-(c) Ground vehicle true and estimated trajectories. (d) Estimated trajectory and the final 95-th percentile uncertainty ellipsoid for one of the Orbcomm satellites. Map data: Google Earth.

### 11.3.2 Aerial Vehicle

An experiment was conducted to evaluate the performance of the LEO-aided INS STAN framework on a UAV. The ground truth trajectory was taken from the UAV's onboard navigation system, which consists of a MEMS IMU, a multi-constellation GNSS receiver (GPS and GLONASS), a pressure altimeter, and a magnetometer. The experimental setup is shown in Figure 33.

The UAV flew a commanded trajectory in Irvine, California, USA, over a 155-second period during which 2 Orbcomm LEO satellites were available (FM 108 and FM 116). Figure 34(a) depicts a skyplot of the satellite trajectories over the course of the experiment. Figure 34(b) shows the Doppler measured by the MATRIX SDR and the estimated Doppler using satellite position and velocity obtained from TLE files and an SGP4 propagator for the 2 Orbcomm satellites.

Three frameworks were implemented to estimate the UAV’s trajectory: (i) the LEO-aided INS STAN framework initialized using TLE files, (ii) the LEO-aided INS STAN framework that used the decoded periodically transmitted LEO satellite positions, which were transmitted by the Orbcomm satellites, and (iii) a traditional GPS-aided INS for comparative analysis. The estimated trajectories were compared with the trajectory extracted from the UAV’s onboard navigation system. Each framework had access to GPS for only the first 125 seconds. Figure 35(a) shows the trajectories that the 2 Orbcomm LEO satellites traversed over the course of the experiment. Figure 35(b)-(d) illustrate the UAV’s true trajectory and those estimated by each of the three frameworks. Table 7 summarizes the final error and position RMSE achieved by each framework after GPS cutoff.

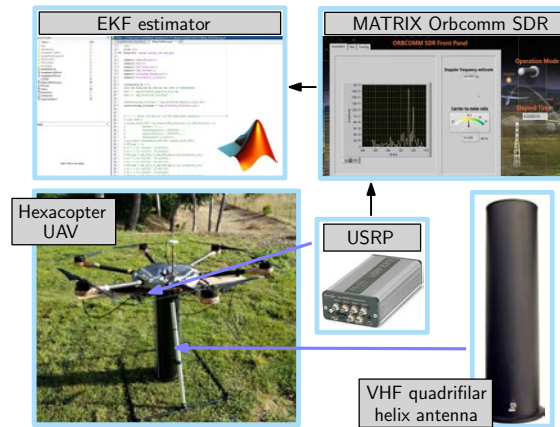


Figure 33: Hardware and software setup for the UAV experiment.

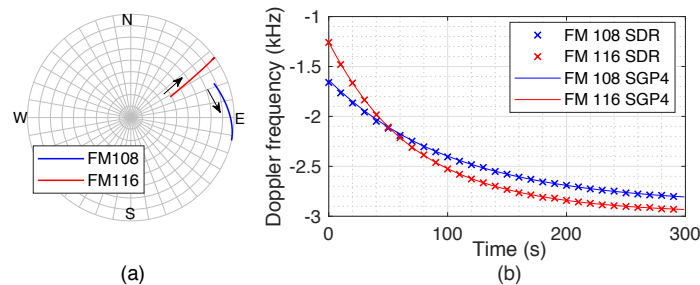


Figure 34: (a) Skyplot of the Orbcomm satellite trajectories. (b) Doppler frequency measurement produced by the MATRIX SDR and the expected Doppler according to an SGP4 propagator for the UAV experiment.

Table 7: Experimental results with 2 Orbcomm LEO satellites for a UAV navigating about 1.53 km in 155 seconds (GPS signals were cut off after the first 125 seconds). These results are after GPS cutoff.

	Unaided INS	LEO-aided INS STAN	LEO-aided INS STAN with periodically transmitted satellite positions
Final Error (m)	123.5	29.9	5.7
RMSE (m)	53.7	15.9	5.4

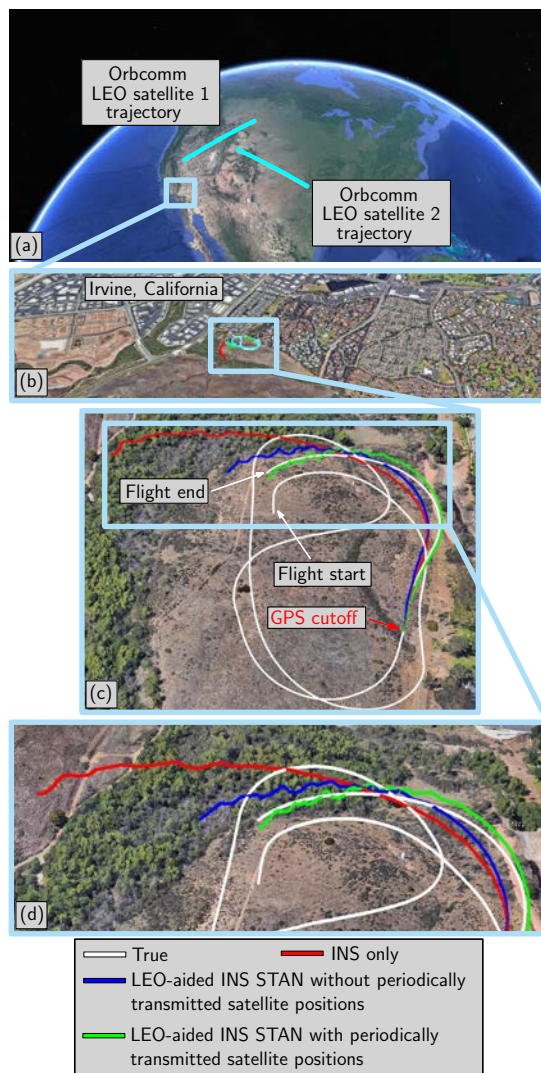


Figure 35: Results of the UAV experiment. (a) Orbcomm satellite trajectories. (b)-(d) UAV's true and estimated trajectories. Map data: Google Earth.

## References

- [1] M. Joerger, L. Gratton, B. Pervan, and C. Cohen, “Analysis of Iridium-augmented GPS for floating carrier phase positioning,” *NAVIGATION, Journal of the Institute of Navigation*, vol. 57, no. 2, pp. 137–160, 2010.
- [2] K. Pesyna, Z. Kassas, and T. Humphreys, “Constructing a continuous phase time history from TDMA signals for opportunistic navigation,” in *Proceedings of IEEE/ION Position Location and Navigation Symposium*, April 2012, pp. 1209–1220.
- [3] T. Reid, A. Neish, T. Walter, and P. Enge, “Broadband LEO constellations for navigation,” *NAVIGATION, Journal of the Institute of Navigation*, vol. 65, no. 2, pp. 205–220, 2018.
- [4] J. Morales, J. Khalife, A. Abdallah, C. Ardito, and Z. Kassas, “Inertial navigation system aiding with Orbcomm LEO satellite Doppler measurements,” in *Proceedings of ION GNSS Conference*, September 2018, pp. 2718–2725.
- [5] R. Landry, A. Nguyen, H. Rasaei, A. Amrhar, X. Fang, and H. Benzerrouk, “Iridium Next LEO satellites as an alternative PNT in GNSS denied environments—part 1,” *Inside GNSS Magazine*, pp. 56–64., May 2019.
- [6] Z. Kassas, J. Morales, and J. Khalife, “New-age satellite-based navigation – STAN: simultaneous tracking and navigation with LEO satellite signals,” *Inside GNSS Magazine*, vol. 14, no. 4, pp. 56–65, 2019.
- [7] J. Morales, J. Khalife, U. S. Cruz, and Z. Kassas, “Orbit modeling for simultaneous tracking and navigation using LEO satellite signals,” in *Proceedings of ION GNSS Conference*, September 2019, pp. 2090–2099.
- [8] T. Reid, A. Neish, T. Walter, and P. Enge, “Leveraging commercial broadband LEO constellations for navigating,” in *Proceedings of ION GNSS Conference*, September 2016, pp. 2300–2314.
- [9] J. Morales, J. Khalife, and Z. Kassas, “Simultaneous tracking of Orbcomm LEO satellites and inertial navigation system aiding using Doppler measurements,” in *Proceedings of IEEE Vehicular Technology Conference*, April 2019, pp. 1–6.
- [10] J. Khalife and Z. Kassas, “Receiver design for Doppler positioning with LEO satellites,” in *Proceedings of IEEE International Conference on Acoustics, Speech and Signal Processing*, May 2019, pp. 5506–5510.
- [11] C. Ardito, J. Morales, J. Khalife, A. Abdallah, and Z. Kassas, “Performance evaluation of navigation using LEO satellite signals with periodically transmitted satellite positions,” in *Proceedings of ION International Technical Meeting Conference*, 2019, pp. 306–318.

- [12] J. Raquet and R. Martin, “Non-GNSS radio frequency navigation,” in *Proceedings of IEEE International Conference on Acoustics, Speech and Signal Processing*, March 2008, pp. 5308–5311.
- [13] L. Merry, R. Faragher, and S. Schedin, “Comparison of opportunistic signals for localisation,” in *Proceedings of IFAC Symposium on Intelligent Autonomous Vehicles*, September 2010, pp. 109–114.
- [14] Z. Kassas, “Collaborative opportunistic navigation,” *IEEE Aerospace and Electronic Systems Magazine*, vol. 28, no. 6, pp. 38–41, 2013.
- [15] Z. Kassas, “Analysis and synthesis of collaborative opportunistic navigation systems,” Ph.D. dissertation, The University of Texas at Austin, USA, 2014.
- [16] T. Hall, C. Counselman III, and P. Misra, “Radiolocation using AM broadcast signals: Positioning performance,” in *Proceedings of ION GPS Conference*, September 2002, pp. 921–932.
- [17] J. McEllroy, “Navigation using signals of opportunity in the AM transmission band,” Master’s thesis, Air Force Institute of Technology, Wright-Patterson Air Force Base, Ohio, USA, 2006.
- [18] S. Fang, J. Chen, H. Huang, and T. Lin, “Is FM a RF-based positioning solution in a metropolitan-scale environment? A probabilistic approach with radio measurements analysis,” *IEEE Transactions on Broadcasting*, vol. 55, no. 3, pp. 577–588, September 2009.
- [19] A. Popleteev, “Indoor positioning using FM radio signals,” Ph.D. dissertation, University of Trento, Italy, 2011.
- [20] I. Bisio, M. Cerruti, F. Lavagetto, M. Marchese, M. Pastorino, A. Randazzo, and A. Sciarrone, “A trainingless WiFi fingerprint positioning approach over mobile devices,” *IEEE Antennas and Wireless Propagation Letters*, vol. 13, pp. 832–835, 2014.
- [21] R. Faragher and R. Harle, “Towards an efficient, intelligent, opportunistic smartphone indoor positioning system,” *NAVIGATION, Journal of the Institute of Navigation*, vol. 62, no. 1, pp. 55–72, 2015.
- [22] J. Khalife, Z. Kassas, and S. Saab, “Indoor localization based on floor plans and power maps: Non-line of sight to virtual line of sight,” in *Proceedings of ION GNSS Conference*, September 2015, pp. 2291–2300.
- [23] J. Wilson, “Automotive WiFi availability in dynamic urban canyon environments,” *NAVIGATION, Journal of the Institute of Navigation*, vol. 63, no. 2, pp. 161–172, 2016.
- [24] M. Rabinowitz and J. Spilker, Jr., “A new positioning system using television synchronization signals,” *IEEE Transactions on Broadcasting*, vol. 51, no. 1, pp. 51–61, March 2005.

- [25] P. Thevenon, S. Damien, O. Julien, C. Macabiau, M. Bousquet, L. Ries, and S. Corazza, “Positioning using mobile TV based on the DVB-SH standard,” *NAVIGATION, Journal of the Institute of Navigation*, vol. 58, no. 2, pp. 71–90, 2011.
- [26] J. Yang, X. Wang, M. Rahman, S. Park, H. Kim, and Y. Wu, “A new positioning system using DVB-T2 transmitter signature waveforms in single frequency networks,” *IEEE Transactions on Broadcasting*, vol. 58, no. 3, pp. 347–359, September 2012.
- [27] C. Gentner, B. Ma, M. Ulmschneider, T. Jost, and A. Dammann, “Simultaneous localization and mapping in multipath environments,” in *Proceedings of IEEE/ION Position Location and Navigation Symposium*, April 2016, pp. 807–815.
- [28] W. Xu, M. Huang, C. Zhu, and A. Dammann, “Maximum likelihood TOA and OTDOA estimation with first arriving path detection for 3GPP LTE system,” *Transactions on Emerging Telecommunications Technologies*, vol. 27, no. 3, pp. 339–356, 2016.
- [29] A. Tahat, G. Kaddoum, S. Yousefi, S. Valaee, and F. Gagnon, “A look at the recent wireless positioning techniques with a focus on algorithms for moving receivers,” *IEEE Access*, vol. 4, pp. 6652–6680, 2016.
- [30] Z. Kassas, J. Khalife, K. Shamaei, and J. Morales, “I hear, therefore I know where I am: Compensating for GNSS limitations with cellular signals,” *IEEE Signal Processing Magazine*, pp. 111–124, September 2017.
- [31] K. Shamaei, J. Khalife, and Z. Kassas, “Exploiting LTE signals for navigation: Theory to implementation,” *IEEE Transactions on Wireless Communications*, vol. 17, no. 4, pp. 2173–2189, April 2018.
- [32] J. Khalife, K. Shamaei, and Z. Kassas, “Navigation with cellular CDMA signals – part I: Signal modeling and software-defined receiver design,” *IEEE Transactions on Signal Processing*, vol. 66, no. 8, pp. 2191–2203, April 2018.
- [33] J. Khalife and Z. Kassas, “Navigation with cellular CDMA signals – part II: Performance analysis and experimental results,” *IEEE Transactions on Signal Processing*, vol. 66, no. 8, pp. 2204–2218, April 2018.
- [34] J. Khalife and Z. Kassas, “Opportunistic UAV navigation with carrier phase measurements from asynchronous cellular signals,” *IEEE Transactions on Aerospace and Electronic Systems*, 2019, accepted.
- [35] C. Yang, T. Nguyen, and E. Blasch, “Mobile positioning via fusion of mixed signals of opportunity,” *IEEE Aerospace and Electronic Systems Magazine*, vol. 29, no. 4, pp. 34–46, April 2014.
- [36] M. Driusso, C. Marshall, M. Sabathy, F. Knutti, H. Mathis, and F. Babich, “Vehicular position tracking using LTE signals,” *IEEE Transactions on Vehicular Technology*, vol. 66, no. 4, pp. 3376–3391, April 2017.

- [37] K. Shamaei and Z. Kassas, “LTE receiver design and multipath analysis for navigation in urban environments,” *NAVIGATION, Journal of the Institute of Navigation*, vol. 65, no. 4, pp. 655–675, December 2018.
- [38] K. Shamaei, J. Khalife, and Z. Kassas, “A joint TOA and DOA approach for positioning with LTE signals,” in *Proceedings of IEEE/ION Position, Location, and Navigation Symposium*, April 2018, pp. 81–91.
- [39] M. Maaref and Z. Kassas, “Ground vehicle navigation in GNSS-challenged environments using signals of opportunity and a closed-loop map-matching approach,” *IEEE Transactions on Intelligent Transportation Systems*, pp. 1–16, June 2019.
- [40] J. Khalife and Z. Kassas, “Precise UAV navigation with cellular carrier phase measurements,” in *Proceedings of IEEE/ION Position, Location, and Navigation Symposium*, April 2018, pp. 978–989.
- [41] J. Khalife, K. Shamaei, S. Bhattacharya, and Z. Kassas, “Centimeter-accurate UAV navigation with cellular signals,” in *Proceedings of ION GNSS Conference*, September 2018, pp. 2321–2331.
- [42] K. Shamaei, , and Z. Kassas, “Sub-meter accurate UAV navigation and cycle slip detection with LTE carrier phase,” in *Proceedings of ION GNSS Conference*, September 2019, pp. 2469–2479.
- [43] J. Khalife, S. Ragothaman, and Z. Kassas, “Pose estimation with lidar odometry and cellular pseudoranges,” in *Proceedings of IEEE Intelligent Vehicles Symposium*, June 2017, pp. 1722–1727.
- [44] M. Maaref, J. Khalife, and Z. Kassas, “Lane-level localization and mapping in GNSS-challenged environments by fusing lidar data and cellular pseudoranges,” *IEEE Transactions on Intelligent Vehicles*, vol. 4, no. 1, pp. 73–89, March 2019.
- [45] J. Morales, P. Roysdon, and Z. Kassas, “Signals of opportunity aided inertial navigation,” in *Proceedings of ION GNSS Conference*, September 2016, pp. 1492–1501.
- [46] Z. Kassas, J. Morales, K. Shamaei, and J. Khalife, “LTE steers UAV,” *GPS World Magazine*, vol. 28, no. 4, pp. 18–25, April 2017.
- [47] K. Shamaei, J. Morales, and Z. Kassas, “Positioning performance of LTE signals in Rician fading environments exploiting antenna motion,” in *Proceedings of ION GNSS Conference*, September 2018, pp. 3423–3432.
- [48] A. Abdallah, K. Shamaei, and Z. Kassas, “Indoor positioning based on LTE carrier phase measurements and an inertial measurement unit,” in *Proceedings of ION GNSS Conference*, September 2018, pp. 3374–3384.
- [49] K. Shamaei, J. Morales, and Z. Kassas, “A framework for navigation with LTE time-correlated pseudorange errors in multipath environments,” in *Proceedings of IEEE Vehicular Technology Conference*, 2019, pp. 1–6.

- [50] A. Abdallah, K. Shamaei, and Z. Kassas, “Performance characterization of an indoor localization system with LTE code and carrier phase measurements and an IMU,” in *Proceedings of International Conference on Indoor Positioning and Indoor Navigation*, October 2019, accepted.
- [51] Z. Kassas, M. Maaref, J. Morales, J. Khalife, and K. Shamaei, “Robust vehicular navigation and map-matching in urban environments with IMU, GNSS, and cellular signals,” *IEEE Intelligent Transportation Systems Magazine*, September 2018, accepted.
- [52] M. Maaref and Z. Kassas, “Measurement characterization and autonomous outlier detection and exclusion for ground vehicle navigation with cellular signals and IMU,” *IEEE Transactions on Intelligent Vehicles*, 2019, submitted.
- [53] J. Morales and Z. Kassas, “Tightly-coupled inertial navigation system with signals of opportunity aiding,” *IEEE Transactions on Aerospace and Electronic Systems*, 2019, submitted.
- [54] D. Lawrence, H. Cobb, G. Gutt, M. OConnor, T. Reid, T. Walter, and D. Whelan, “Navigation from LEO: Current capability and future promise,” *GPS World Magazine*, vol. 28, no. 7, pp. 42–48, July 2017.
- [55] Federal Communications Commission, “FCC boosts satellite broadband connectivity and competition in the united states,” <https://www.fcc.gov/document/fcc-boosts-satellite-broadband-connectivity-competition>, November 2018, accessed October 2, 2019.
- [56] J. Vetter, “Fifty years of orbit determination: Development of modern astrodynamics methods,” *Johns Hopkins APL Technical Digest*, vol. 27, no. 3, pp. 239–252, November 2007.
- [57] North American Aerospace Defense Command (NORAD), “Two-line element sets,” <http://celestrak.com/NORAD/elements/>.
- [58] D. Vallado, “An analysis of state vector propagation using differing flight dynamics programs,” in *Proceedings of the AAS Space Flight Mechanics Conference*, vol. 120, January 2005.
- [59] D. Qiu, D. Lorenzo, and T. Bhattacharya, “Indoor geo-location with cellular RF pattern matching and LEO communication satellite signals,” in *Proceedings of ION International Technical Meeting Conference*, January 2013, pp. 726–733.
- [60] X. Chen, M. Wang, and L. Zhang, “Analysis on the performance bound of Doppler positioning using one LEO satellite,” in *Proceedings of IEEE Vehicular Technology Conference*, May 2016, pp. 1–5.
- [61] J. Zhao, L. Li, and Y. Gong, “Joint navigation and synchronization in LEO dual-satellite geolocation systems,” in *Proceedings of IEEE Vehicular Technology Conference*, June 2017, pp. 1–5.

- [62] J. Morales, J. Khalife, and Z. Kassas, “Collaborative autonomous vehicles with signals of opportunity aided inertial navigation systems,” in *Proceedings of ION International Technical Meeting Conference*, January 2017, 805–818.
- [63] J. Morales and Z. Kassas, “Distributed signals of opportunity aided inertial navigation with intermittent communication,” in *Proceedings of ION GNSS Conference*, September 2017, pp. 2519–2530.
- [64] J. Morales and Z. Kassas, “Information fusion strategies for collaborative radio SLAM,” in *Proceedings of IEEE/ION Position Location and Navigation Symposium*, April 2018, pp. 1445–1454.
- [65] J. Morales and Z. Kassas, “A low communication rate distributed inertial navigation architecture with cellular signal aiding,” in *Proceedings of IEEE Vehicular Technology Conference*, 2018, pp. 1–6.
- [66] Z. Kassas, “Position, navigation, and timing technologies in the 21st century,” J. Morton, F. van Diggelen, J. Spilker, Jr., and B. Parkinson, Eds. Wiley-IEEE, 2019, vol. 2, ch. 37: Navigation with cellular signals.
- [67] J. Khalife and Z. Kassas, “Assessment of differential carrier phase measurements from orbcomm LEO satellite signals for opportunistic navigation,” in *Proceedings of ION GNSS Conference*, September 2019, pp. 4053–4063.
- [68] P. Misra and P. Enge, *Global Positioning System: Signals, Measurements, and Performance*, 2nd ed. Ganga-Jamuna Press, 2010.
- [69] B. Tapley, M. Watkins, C. Ries, W. Davis, R. Eanes, S. Poole, H. Rim, B. Schutz, C. Shum, R. Nerem, F. Lerch, J. Marshall, S. Klosko, N. Pavlis, and R. Williamson, “The joint gravity model 3,” *Journal of Geophysical Research*, vol. 101, no. B12, pp. 28 029–28 049., December 1996.
- [70] J. Vinti, *Orbital and Celestial Mechanics*. American Institute of Aeronautics and Astronautics, 1998.
- [71] R. Brown and P. Hwang, *Introduction to Random Signals and Applied Kalman Filtering*, 3rd ed. John Wiley & Sons, 2002.
- [72] N. JPL, “Ionospheric and atmospheric remote sensing,” <https://iono.jpl.nasa.gov/>, accessed October 1, 2019.
- [73] Orbcomm, <https://www.orbcomm.com/en/networks/satellite>, accessed September 30, 2018.
- [74] M. Rice, C. Dick, and F. Harris, “Maximum likelihood carrier phase synchronization in FPGA-based software defined radios,” in *Proceeding of IEEE International Conference on Acoustics, Speech, and Signal Processing*, vol. 2, May 2001, pp. 889–892.

- [75] Y. Yang, J. Lie, and A. Quintero, “Low complexity implementation of carrier and symbol timing synchronization for a fully digital downhole telemetry system,” in *Proceedings of IEEE International Conference on Acoustics, Speech, and Signal Processing*, April 2018, pp. 1150–1153.
- [76] N. Levanon, “Quick position determination using 1 or 2 LEO satellites,” *IEEE Transactions on Aerospace and Electronic Systems*, vol. 34, no. 3, pp. 736–754, July 1998.
- [77] N. Nguyen and K. Dogancay, “Algebraic solution for stationary emitter geolocation by a LEO satellite using doppler frequency measurements,” in *Proceedings of IEEE International Conference on Acoustics, Speech and Signal Processing*, March 2016, pp. 3341–3345.
- [78] J. Hamkins and M. Simon, *Autonomous software-defined radio receivers for deep space applications*. New York, NY: John Wiley & Sons, Inc, 2006, ch. 8, pp. 227–270.
- [79] A. Oppenheim, W. Ronald, and R. John, *Discrete-time signal processing*, 3rd ed. Englewood Cliffs, NJ: Prentice hall, 2009, ch. 9, pp. 693–718.
- [80] Autonomous Systems Perception, Intelligence, and Navigation (ASPIN) Laboratory, <http://www.aspin.ucr.edu>.
- [81] SpaceX, “FCC File Number: SATLOA2016111500118,” *IB FCC Report*, March 2018, accessed: November 29, 2018.
- [82] SpaceX, “FCC File Number: SATLOA2017030100027,” *IB FCC Report*, November 2018, accessed: November 29, 2018.
- [83] SpaceX, “FCC File Number: SATMOD2018110800083,” *IB FCC Report*, November 2018, accessed: November 29, 2018.
- [84] UNOOSA, “Online index of objects launched into outer space,” <http://www.unoosa.org/oosa/osoindex/>, November 2018, accessed: November 29, 2018.
- [85] Z. Kassas and T. Humphreys, “Observability analysis of collaborative opportunistic navigation with pseudorange measurements,” *IEEE Transactions on Intelligent Transportation Systems*, vol. 15, no. 1, pp. 260–273, February 2014.
- [86] Z. Kassas and T. Humphreys, “Receding horizon trajectory optimization in opportunistic navigation environments,” *IEEE Transactions on Aerospace and Electronic Systems*, vol. 51, no. 2, pp. 866–877, April 2015.
- [87] J. Morales and Z. Kassas, “Stochastic observability and uncertainty characterization in simultaneous receiver and transmitter localization,” *IEEE Transactions on Aerospace and Electronic Systems*, vol. 55, no. 2, pp. 1021–1031, April 2019.
- [88] J. Farrell and M. Barth, *The Global Positioning System and Inertial Navigation*. New York: McGraw-Hill, 1998.

- [89] A. Thompson, J. Moran, and G. Swenson, *Interferometry and Synthesis in Radio Astronomy*, 2nd ed. John Wiley & Sons, 2001.
- [90] P. Groves, *Principles of GNSS, Inertial, and Multisensor Integrated Navigation Systems*, 2nd ed. Artech House, 2013.
- [91] D. Vallado and P. Crawford, “SGP4 orbit determination,” in *Proceedings of AIAA/AAS Astrodynamics Specialist Conference and Exhibit*, August 2008.
- [92] A. Brandao, L. Lopes, and D. McLemon, “In-service monitoring of multipath delay and cochannel interference for indoor mobile communication systems,” in *Proceedings of IEEE ICC/SUPERCOMM*, vol. 3, May 1994, pp. 1458–1462.